2014

Thermal Properties of Magnetic Nanoparticles In External AC Magnetic Field

Anna Beata Lukawska
Wright State University

THERMAL PROPERTIES OF MAGNETIC NANOPARTICLES IN EXTERNAL AC MAGNETIC FIELD

A thesis submitted in partial fulfillment of
the requirements for the degree of
Master of Science

By

Anna Beata Lukawska
B.S. in Physics, University of Southern Denmark, 2010

2014
Wright State University

WRIGHT STATE UNIVERSITY

GRADUATE SCHOOL

April 16, 2014

I HEREBY RECOMMEND THAT THE THESIS PREPARED UNDER MY SUPERVISION BY Anna Beata Lukawska ENTITLED Thermal properties of magnetic nanoparticles in external ac magnetic field BE ACCEPTED IN PARTIAL FULFILLMENT OF THE REQUIREMENTS FOR THE DEGREE OF Master of Science.

_____
Gregory Kozlowski, PhD
Thesis Director

_____
Doug Petkie, PhD
Chair, Physics Department
College of Science & Mathematics

Committee on Final Examination

_____
Gregory Kozlowski, PhD

_____
Doug Petkie, PhD

_____
David Miller, PhD

_____
Robert Fyffe, PhD
Vice President for Research and Dean
of the Graduate School

ABSTRACT

Lukawska, Anna Beata, M.S., Department of Physics, Wright State University, 2014.
Thermal properties of magnetic nanoparticles in external ac magnetic field.

This work studies thermal properties of magnetic nanoparticles in an external ac magnetic field. Dried iron and cobalt nanoparticles were prepared by thermal decomposition of iron pentacarbonyl ($Fe(CO)_5$) and dicobalt octacarbonyl ($Co_2(CO)_8$), triscobalt nona(carbonyl)chloride ($Co_3(CO)_9Cl$), or tetracaobalt dodecacarbonyl ($Co_4(CO)_{12}$) [1]. The samples had different mean diameters: *5.6 – 21.4 nm* for iron and *6.5 – 19.4 nm* for cobalt. Each sample was exposed to ac magnetic field and the increase in temperature of the sample was measured. Results were analyzed to find the critical diameters for the transitions from multi-domain to single-domain and from single-domain to superparamagnetic regime. The nanoparticles were analyzed for their possible application for hyperthermia cancer treatment. Due to this application and to broaden the understanding of how magnetic nanoparticles would influence human tissue, a mathematical model written in Matlab and based on bio-heat equations was introduced.

TABLE OF CONTENTS

LIST OF FIGURES

LIST OF TABLES

ACKNOWLEDGEMENTS

I would like to thank my family and fiancé for supporting me every single day. I know how much it means to my parents and my brother that I am graduating with a Master degree. My family supported me all my life, and the day of my graduation will be a huge celebration. Love and care from my fiancé was lifting me up every single time I thought that I could not write anymore.

At Wright State University, I would like to give my thanks for all the assistance from Dr. Gregory Kozlowski, and his time and patience in helping me through the research and thesis process. I have learned so much from Dr. Kozlowski and it had been a pleasure working under him. I want to thank Dr. Petkie for agreeing to be on my committee, being very supportive, encouraging me to finish my degree despite difficulties, and making it possible even it seemed otherwise. I also would like to thank Dr. Miller for all the time he spent with me discussing mathematical and programming challenges I was encountering and for being a member of my committee.

DEDICATION

I dedicate this thesis to my parents Beata Anna Lukawska and Miroslaw Slawomir Lukawski. They waited for this very long, and they have given me so much love support and strength that I would never be able to express my gratitude. I can only hope to pass forward all the love I have gotten when one day I will have the honor of being a parent myself.

INTRODUCTION

The modern race of miniaturization, mobility, and accessibility brought us knowledge about how to produce, control, manipulate, and use nanomaterials. Nanomaterials are broadly defined as materials that have at least one dimension less than 100 nm. A more strict definition is connected with the fact that nanomaterials are built from a small amount of atoms, their masses are small, and they have a very high surface to volume ratios because of the fine grain sizes. Therefore, nanomaterials are materials with properties inherently dependent on their size. Furthermore, due to their small size, quantum effects have to be considered when analyzing them. For example, while metal particles are becoming smaller, their electronic conduction band gradually changes from continuous characteristic for bulk materials into discrete states that are an atomic property. By the virtue of nanoscience which is a very active field over the last few decades the understanding of the size dependent properties of materials is getting better, and they are being exploited in an abundance of applications from fundamental studies to various fields like electronics, optics, agriculture, oil recovery or medicine.

The goal of this project is to acquire theoretical and experimental understanding of how the magnetic properties vary with the size of the nanomaterials. Meanwhile, we try to acquire an understanding what requirements the investigated magnetic nanomaterials have to fulfill to be a promising candidate for application in magnetic nanoparticle based hyperthermia treatment. Hyperthermia is a method of fighting diseases like for example cancer by increasing temperature. Potential usage of the magnetic nanoparticles for the tumor therapy could make the treatment very localized. Targeting only mutated cells,

makes it almost side effect free if the particles are biocompatible with human body. Magnetic nanomaterials used in this study were prepared by collaborators at the Cambridge University in England, dried to a powder and sent to Wright State University (WSU).

The samples were prepared by thermal decomposition of iron pentacarbonyl ($Fe(CO)_5$) to produce iron nanoparticles and dicobalt octacarbonyl ($Co_2(CO)_8$), triscobalt nona(carbonyl)chloride ($Co_3(CO)_9Cl$), or tetracaobalt dodecacarbonyl ($Co_4(CO)_{12}$) to produce cobalt nanoparticles [1]. The produced iron and cobalt nanoparticles batches have different mean diameters: *5.6 – 21.4 nm* for iron and *6.5 – 19.4 nm* for cobalt. We aim to find, predicted by the theory, the dependence of the specific loss power (SLP) on the diameter of the particles in a spherical shape approximation. This project also aims to find the critical diameter values for the transitions from multi-domain to single-domain and from single-domain to superparamagnetic regime for iron and cobalt. Single domain particles have a magnetization, which do not vary across it. Above critical diameter nanoparticles divide into domains. The nanoparticles are superparamagnetic when thermal fluctuations can randomly change direction of its single domain magnetization.

Initially, this project examines if the samples of nanomaterials produce thermal energy when placed in an ac magnetic field, and plots it compare to particle diameter. Secondly, an examination of the rise in temperature in the vicinity of nanoparticles, caused by the released energy, is satisfactory to raise a human body's temperature by *6-8°C*. Such a change in temperature is needed for human body of *37°C* to achieve approximately *45°C*, which is a destruction temperature for cancerous cells. Iron and cobalt are expected to

produce more heat than the widely used iron oxide [29], and this project aims to verify this.

Results obtained from experiments are analyzed with respect to application in hyperthermia treatment of cancer. The goal is to create the smallest samples of magnetic nanoparticles with the highest possible specific loss power. Due to hyperthermia being a possible future application of the analyzed nanoparticles, the idea came through this study to construct a mathematical model in Matlab based on bio-heat equations for spherical tumor surrounded by healthy tissue. By solving those equations, the model gives a temperature dependence on time and radius from the center of the tumor. This gives an understanding of how heat produced by nanoparticles evenly distributed within a tumor increases temperature of the tumor itself, but also how it spreads and heats neighboring healthy tissue cells.

Chapter one, Theoretical Background, first summarizes how ferromagnetic materials properties change with decreasing size, and it gives a review of critical size phenomena and discusses transitions from multi–domain to single domain and from single–domain to superparamagnetic phase. A lot of properties of the materials at the nanoscale depend on their shape, but in this study for simplicity the discussion is conducted using an approximation of spherical nanoparticles. Secondly, Chapter one reviews different mechanisms of heat generation by nanoparticles placed in an ac magnetic field, and the dominance of those mechanisms in different size ranges based on critical diameters definitions. Lastly, the Chapter briefly describes hyperthermia treatment as a reason for the usage of mathematical models, for the heat transfer from

spherical tumor, volumetrically covered with uniformly distributed magnetic nanoparticles, to healthy tissue.

Chapter two, called Materials, Methods, and Procedures, first examines the synthesis procedures, and some of the properties, for iron and cobalt nanoparticles and their sizes. Secondly, it presents the method used to measure temperature changes in iron and cobalt samples, with different size distributions, when placed in an ac magnetic field. Thirdly, a description is given of the calculation of the specific loss power (SLP) of the nanoparticles when the ac magnetic field is known, and also the specific loss power per mass of the sample (SPL'). Lastly, the bio-heat equations used for constructing a mathematical model in Matlab are presented.

Chapter three, Results and Discussion, examines the results of the heat measurements. The heating curves for some of the samples of both iron and cobalt, and the SLP' dependence on the diameter for both types of nanoparticles are shown, and comparison of results with iron oxide is done. Secondly, the preliminary bio-heat model results are mentioned.

The final chapter, Chapter four, summarizes the results and what was achieved during this master study. It also offers ideas for further research and development.

1. THEORETICAL BACKGROUND

1.1 MAGNETISM

Electricity and magnetism are unified in equations gathered and polished by James Clark Maxwell,

$$\nabla \cdot \vec{E} = \frac{\rho}{\epsilon_0}, \tag{1}$$

$$\nabla \cdot \vec{B} = 0, \tag{2}$$

$$\nabla \times \vec{E} = -\frac{\partial \vec{B}}{\partial t}, \tag{3}$$

$$\nabla \times \vec{B} = \mu_0 \vec{J} + \mu_0 \varepsilon_0 \frac{\partial \vec{E}}{\partial t}. \tag{4}$$

Eq.1 is called Gauss's law, and it shows how the electric field $\vec{E}$ diverges from the charge density ρ. ε_0 is the permittivity of free space. Eq. 2 is Gauss's law for magnetism, where $\vec{B}$ is the magnetic induction, which assumes no magnetic monopoles. However, in 2013 a group from the University of Cologne [2] has produced artificial magnetic monopoles resembling those postulated in 1931 by Paul Dirac. Eq. 3 is called Faraday's law of induction and represents how a time varying magnetic field produces an electric field. To describe magnetic monopoles both Eqs. 2 and 3 would have to be modified. Eq. 4 is Ampere's circuit law describing how an electric current density $\vec{J}$ and a time varying electric field produce a magnetic field. In Eq. 4, μ_0 is the magnetic permeability of free space, which is the measure of the ability to support the magnetic field formation by a material [3]. The magnetization $\vec{M}$ is the vector field describing the density of permanent

or induced magnetic dipole moments in a material [4]. Classically [5], the magnetic moment $\vec{\mu}$ is defined through a current *I* around a small area *dA*:

$$d\vec{\mu} = I\, d\vec{A}. \tag{5}$$

The origin of the magnetic moments creating magnetization of the material can either be the orbital motion of the electron, or the spin of the electron. The magnetization $\vec{M}$ results from the response of the material to the externally applied magnetic field and unbalanced magnetic dipole moments due to intrinsic properties of the material itself. The magnitude of the magnetization $\vec{M}$ [5], is equal to the total magnetic moment per unit volume:

$$M = \mu \frac{N}{V}. \tag{6}$$

In vacuum, magnetization does not occur. When a material is placed in an external magnetic field $\vec{H}$, the induced magnetization is created

$$\vec{M} = \chi \vec{H}, \tag{7}$$

where the proportionality constant χ is called the magnetic susceptibility of the material

$$\chi = \frac{\mu}{\mu_0} - 1. \tag{8}$$

Eq. 7 is true only if the material is assumed to be magnetically isotropic. This means that the material has no preferential direction for its magnetic moment. However, real crystals are anisotropic, which is when the magnetic moment of the material depends on the direction within the structure of the material, and it will self-align along an energetically favorable direction called an easy axis. Most common types of anisotropies are: the magneto-crystalline anisotropy where the crystallographic directions define the easy axes,

and the shape anisotropy, important in non-spherical small particles where the easy axis is an axis along longest dimension. The response of a material to an external magnetic field $\vec{H}$ is called the magnetic induction $\vec{B}$,

$$\vec{B} = \mu(\vec{H} + \vec{M}) = \mu_0(1 + \chi)\vec{H} = \mu_0\mu_r\vec{H}, \quad (9)$$

where $\mu_r = 1 + \chi$ is the relative permeability (for vacuum $\mu_r = 1$).

The Bohr-van Leeuwen theorem [5] shows that when calculating an average of the magnetic moment, the partial derivative of the classical partition function Z with respect to magnitude of the magnetic induction $\vec{B}$ arises,

$$\langle\mu\rangle = \frac{kT}{Z} \cdot \frac{\partial Z}{\partial B}, \quad (10)$$

and since the partition function does not depend on the magnetic induction, the classical calculation of the average magnetic moment will always give zero. Therefore the classical mechanics and statistical mechanics solely cannot account for magnetism in solids, because magnetism is a quantum mechanical effect.

1.1.1 TYPES OF MAGNETISM

By the means of the susceptibility χ magnetism can be classified into three groups: diamagnetism, paramagnetism, and collective magnetism [5].

1.1.1.1 DIAMAGNETISM

The Hamiltonian H_0 of a single atom that contains Z electrons is a sum of kinetic and potential energies, given by

$$H_0 = \sum_{i=1}^{Z} \left(\frac{p_i^2}{2m} + V_i \right). \quad (11)$$

In the presence of magnetic field, the Hamiltonian is modified to

$$H = H_0 + H_1, \quad (12)$$

where the H_1 represents the modification that can be divided into the paramagnetic term H_1^{para} and the diamagnetic term H_1^{dia}

$$H_1 = H_1^{para} + H_1^{dia} = \mu_B \left(\vec{L} + g\vec{S} \right) \cdot \vec{B} + \frac{e^2}{8m} \sum_{i=1}^{Z} \left(\vec{B} \times \vec{r_i} \right)^2, \quad (13)$$

g is a g-factor of an electron ($g \approx 2$), $\vec{S}$ is the electron spin angular momentum, $\vec{L}$ is the orbital angular momentum, $\mu_B = e\hbar/2m$ is the Bohr magneton, r_i is the orbital radius of electron, and e is the electric charge of the electron. All materials exhibit diamagnetism. If all electronic shells of an atom are filled, then the orbital and spin angular momentum vanish, $L = S = 0$, and the paramagnetic term H_1^{para} is zero [5].

Assuming that the external field $\vec{B}$ is parallel to the z-axis, $\vec{B} = (0,0,B_z)$ we have

$$\left(\vec{B} \times \vec{r_i} \right)^2 = B^2 (x_i^2 + y_i^2), \quad (14)$$

and consequently an energy shift of the ground state is:

$$\Delta E_0 = \frac{e^2 B^2}{8m} \sum_i \langle 0 | x_i^2 + y_i^2 | 0 \rangle, \quad (15)$$

where $|0\rangle$ is the wave function of the ground state. From the spherical symmetry of the atom in the ground state with filled electron shells it can be written that

$$\langle x_i^2 \rangle = \langle y_i^2 \rangle = \langle z_i^2 \rangle = \frac{1}{3} \langle r_i^2 \rangle, \quad (16)$$

so that ΔE_0 can be simplified to

$$\Delta E_0 = \frac{e^2B^2}{12m}\sum_i \langle 0|r_i^2|0\rangle. \quad (17)$$

The magnetic moment of a single atom is

$$\mu = -\frac{\partial F}{\partial B}, \quad (18)$$

where F is the Helmholtz free energy $F = E - TS$, E is the internal energy, T is the temperature and S is the entropy. For $T = 0$ and using Eq. 6 the magnitude of the magnetization $\vec{M}$ is

$$M = \left(-\frac{\partial \Delta E_0}{\partial B}\right)\frac{N}{V} = -\frac{N}{V}\frac{e^2B}{6m}\sum_i \langle r_i^2\rangle. \quad (19)$$

On the other hand, $\vec{M} = \chi\vec{H}$, and $\vec{H} = \vec{B}/\mu_0$, so the susceptibility is

$$\chi = \frac{\vec{M}}{\vec{H}} = \frac{\mu_0\vec{M}}{\vec{B}} = -\frac{N}{V}\frac{\mu_0 e^2}{6m}\sum_i \langle r_i^2\rangle. \quad (20)$$

Thus, for the diamagnetic materials the magnetic susceptibility χ_{dia} is negative. It is also usually a very small quantity. The negative value of the susceptibility means that in an applied magnetic field, diamagnetic materials acquire magnetization that is pointed opposite to the applied field [6]. In diamagnetic materials the susceptibility nearly has a constant value independent of temperature [7]. Diamagnetism is purely an induction effect. An applied externally magnetic field $\vec{H}$ induces in a material magnetic dipoles that are oriented antiparallel with respect to the excitation field due to Lenz's rule [5]. Therefore, the diamagnetic susceptibility is negative $\chi_{dia} < 0$. Diamagnetism is a property of all materials, but it is only relevant in the absence of paramagnetism and collective magnetism. Diamagnetism is associated with the tendency of electrical charges partially

to shield the interior of a body from an applied magnetic field [7]. From Lenz's law, we know that when the magnetic energy flux through an electrical circuit is changed, an induced current is set up in such a direction to oppose the flux change, which explains the minus sign in equation for the diamagnetic susceptibility. Diamagnetism can be found in ionic crystals and crystals composed of inert gas atoms, because these substances have atoms or ions with complete electronic shells [8]. Noble metals are known diamagnetic materials like for example mercury.

1.1.1.2 PARAMAGNETISM

Without an external field no favored orientation of the magnetic moments within material occurs and the resulting magnetization tends to zero. However, an applied field produces a net magnetization in the preferential orientation. Paramagnetic substances have a net angular momentum due to permanent magnetic dipoles arising from unpaired electrons. The magnetic moments can be of localized or itinerant nature [5]. The electrons of an inner shell that is only partially filled cause the localized moments, for instance: *4f* electrons in rare earth metals, or *5f* electrons in actinides [5]. Materials with localized moments exhibit the Langevin paramagnetism. The Langevin susceptibility, $\chi^{Langevin}(T)$, depends on temperature, and at high temperatures follows the Curie law, $\chi^{Langevin}(T) = C/T$, where C is the Curie constant. On the other hand, the itinerant moments are arising from nearly free electrons in the valence band and create so-called Pauli paramagnetism. The susceptibility χ^{Pauli} is almost independent on temperature, and much smaller than $\chi^{Langevin}$. Not going into details of derivation (it can be seen in [5]) lets go through few facts needed to derive a susceptibility relation for Langevin paramagnetism. If the atoms in a solid have non-filled electronic shells the second term in

the Hamiltonian given by Eq. 13 is much smaller than the first one and therefore it can be ignored [8]. The classical moments are substituted by the quantum mechanical total angular momentum $\vec{J} = \vec{L} + \vec{S}$, which is equal to integer or half of an integer value. $\vec{J}$ is defined by the eigenvalue of the J^2, which is $J(J+1)$. The partition function is

$$Z = \sum_{m_J=-J}^{J} e^{\frac{E}{kT}}, \tag{21}$$

where $E=gm_J\mu_B B$ is the energy. Setting $x=g\mu_B B/kT$, the average magnetic moment is

$$\langle m_J \rangle = \frac{\sum m_J e^{xm_J}}{\sum e^{xm_J}} = \frac{1}{Z}\frac{\partial Z}{\partial x}. \tag{22}$$

The saturation magnetization $\vec{M}_S$ is reached if all magnetic moments are parallel, $\vec{M}_S = ng\mu B\vec{J}$. The magnitude of the magnetization $\vec{M}$ along $\vec{B}$ is

$$M = ng\mu_B\langle m_J \rangle = \frac{ng\mu_B}{Z}\frac{\partial Z}{\partial x}. \tag{23}$$

The relative magnetization is proportional to the Brillouin function B_J,

$$\frac{\vec{M}}{\vec{M}_S} = B_J(xJ). \tag{24}$$

For low magnetic fields and not too low temperatures $xJ << 1$, and $B_J(xJ) \approx (J+1)x/3$. Therefore, the paramagnetic susceptibility can be written as

$$\chi = \frac{\mu_0\vec{M}}{\vec{B}} = \frac{\mu_0\vec{M}_S B_J(xJ)}{\vec{B}} = \frac{n}{3}\frac{\mu_0 g_J^2\mu_B^2 J(J+1)}{k_B T} = \frac{C}{T}, \tag{25}$$

where J is the total angular momentum, g is the Lande factor, n is the number of magnetic moments, μ_B is the Bohr magneton, T is the temperature, and $k_B = 1.38\cdot10^{-23} J/K$

is the Boltzmann's constant. *C/T* is, as mentioned before, the classical Curie's law. For larger magnetic fields saturation is reached so that $J(J+1) \sim J^2$, and we can write

$$\chi = \frac{n}{3}\frac{\mu_0 g_J^2 \mu_B^2 J^2}{k_B T}. \quad (26)$$

The susceptibility for paramagnetic materials is highly dependent on the temperature. The permeability of paramagnetic materials decreases at high temperatures because of the randomizing effect of thermal excitations [9]. In summary, the Langevin paramagnetic substances have a positive magnetic susceptibility that depends inversely on the temperature, $\chi_{para}(T) > 0$ [5]. Thus paramagnetic materials become more magnetic at lower temperatures.

1.1.1.3 COLLECTIVE MAGNETISM

The collective magnetism is a result of an exchange interaction between permanent magnetic dipoles that can solely be explained by quantum mechanics [5]. For materials showing collective magnetism, a critical temperature occurs that is characterized by the observation of a spontaneous magnetization being present below it. The magnetic dipoles exhibit an orientation that is not enforced by an external magnetic field. The magnetic moments can be localized or itinerant similarly as for paramagnetic materials. However, the susceptibility exhibits a significantly more complicated dependence of different parameters compared to dia- and paramagnetism. Collective magnetism is divided into: ferromagnetism, ferrimagnetism, and antiferromagnetism. Particles used in this project are made of ferromagnetic materials: iron and cobalt.

1.1.1.3.1 FERROMAGNETISM

Ferromagnetic substances show spontaneous magnetization. The magnetization exists even in the absence of an external magnetic field. Ferromagnetism involves the parallel alignment of the significant fraction of the molecular magnetic moments in some favorable direction in a crystal (anisotropy) [10]. At zero temperature all moments are aligned parallel. The ferromagnetism appears below a critical temperature T_c, called the Curie temperature, which depends on the material. Above this temperature materials are paramagnetic since the magnetic moments have random orientation, and below it materials exhibit permanent magnetism due to the magnetic moments being highly ordered. The ferromagnetism is related to the unfilled *3d* and *4f* energy shells [10].

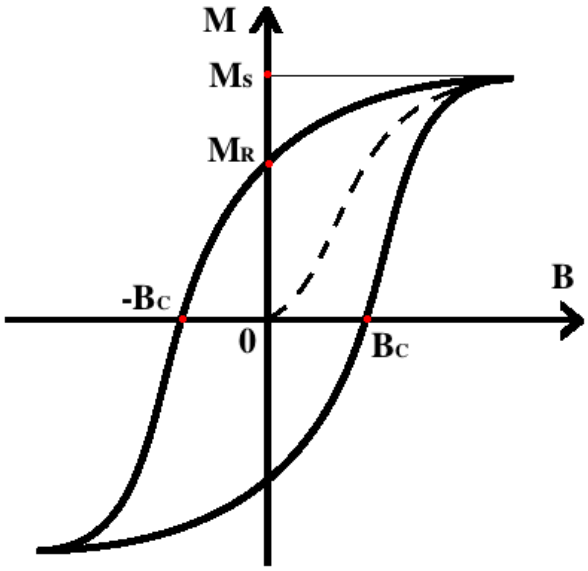

Figure 1. Hysteresis loop.

Starting from zero point in Fig. 1, under an external magnetic field $\vec{B}$, a ferromagnetic material will gradually increase its magnetization, following the dashed curve in Fig. 1

called the initial magnetization curve. At first the increase will be rapid, but then it will slow down and finally reach a constant value at saturation point for which the magnetization reaches its maximum value, the saturation magnetization M_S (spontaneous magnetization). If the field $\vec{B}$ is decreasing, the magnetization $\vec{M}$ decreases slowly following the curve above the initial curve [10]. When $\vec{B}$ reaches zero, magnetization $\vec{M}$ has non-zero value called the remnant magnetization M_R. In order to decrease the magnetization to zero, one has to apply a field in the opposite direction called the coercive field $\vec{B}_C$. A further increase in the coercive field (coercivity) will result in saturation magnetization in opposite direction. Similar scenario can be repeated but in opposite direction to finally close the loop, which is called a hysteresis loop of magnetization.

The area surrounded by the hysteresis loop is a measure of the magnetic hysteresis energy, which has to be applied to reverse the magnetization. A microscopically large region with all the magnetic moments aligned is called a domain. The boundary between two neighbored domains is called the domain wall. Ferromagnetic materials break into domains that align themselves in such a manner to minimize the overall energy of the material [9]. Within each domain the magnetization is uniform and equal to the saturation magnetization, M_S. The different domains are magnetized in different directions. Therefore, the average magnetization of the material is not equal to the spontaneous magnetization and can even be equal to zero for the specific domain configuration. The most common domain wall is a *180°* wall that represents the boundary between domains with opposite magnetization. Within this category there are two classes of walls: Bloch

wall and Neel wall. In the Bloch wall the rotation of the magnetization occurs in a plane parallel to the plane of the domain wall. In the Neel wall the rotation of the magnetization vector takes place in a plane perpendicular to the plane of the domain wall. The domain wall width parameter Δ characterizes the width of the transition region between two magnetic domains [5]. It is given, as a function of the exchange stiffness constant A and the uniaxial anisotropy constant K, by

$$\Delta = \sqrt{\frac{A}{K}}. \tag{27}$$

The domain wall width is given by $\delta_0 = \pi\Delta$. The domain wall energy is also related to the same parameters A and K. In the simple case of the 180° wall of a cubic crystal, the energy per unit area of the wall is

$$\gamma = 4\sqrt{AK}. \tag{28}$$

Bulk magnetic materials consist of uniformly magnetized domains separated by domain walls [10]. The formation of the domain walls is a process driven by the balance between the magnetostatic energy (E_{MS}), which increases proportionally to volume of the materials, and the domain-wall energy (E_{DW}), proportional to the interfacial area between domains [11]. The resultant magnetization of the magnetic materials as a function of the externally applied magnetic field below Curie temperature is characterized by the most important material constant called coercivity $H_c = B_c/\mu_0\mu_r$ [12]. The coercivity increases monotonically with a decreasing diameter D of nanoparticles. However, there is a maximum when nanoparticles enter so-called single-domain regime (see, Fig. 2) and then it decreases. This is of great importance for this project, since heat generated by

nanoparticles should maximize for the same diameter.

1.1.1.3.2 FERRIMAGNETISM

The lattice describing a ferromagnetic material decays into two ferromagnetic sublattices, and the sum of the magnetization of those two sublattices is different than zero. An antiparallel orientation of the magnetization between both sublattices will then be present. Neighboring dipole moments point in opposite directions, but they are not equal in magnitude so they do not balance each other completely, and there is a finite net magnetization below the Curie temperature [10]. An example of a ferromagnetic material is magnetite, Fe_3O_4 or $FeO{\cdot}Fe_2O_3$. Sometimes there is also another temperature below the Curie temperature, called the Neel temperature, which corresponds to the magnetization compensation point where both sublattices have an equal magnitude of magnetization, the net magnetization is zero, and the material is then antiferromagnetic. An external field causes the anisotropy of ferrimagnetic materials, and therefore the rocks of this type are used in the study of geomagnetic properties of Earth (paleomagnetism).

1.1.1.3.3 ANTIFERROMAGETISM

Antiferromagnetism is a special case of ferrimagnetism that exists with no external magnetic field applied. However, it vanishes at and above the critical Neel temperature T_N [14]. A sum of the magnetizations of the material's two sublattices is equal zero. Above the Neel temperature the materials is typically paramagnetic. In a magnetic field an antiferromagnetic material may display a ferromagnetic behavior. Antiferromagnetic materials occur among oxides, an example is nickel oxide NiO.

1.2 NANOMAGNETISM

Nanomagnetism has many fields of application such as geology, in magnetic recording, or in medicine for drug delivery or magnetic hyperthermia. Nanomaterials due to their small sizes exhibit different magnetic behaviors and properties than bulk materials. Those differences arise from the limiting sizes of the magnetic domains, the higher proportion of surface atoms, strong interactions with immediate neighboring materials, and the enhanced importance of thermal fluctuations on the dynamical behavior. The contribution of the surface atoms to the physical properties increases with decreasing sample sizes [15]. This is obvious since the area of the surface of the samples varies typically as $\sim r^2$, while the volume of the samples varies as $\sim r^3$. As a consequence, the ratio of surface to volume varies roughly speaking as r^{-1}. Therefore, the surface to volume ratio increases with decreasing sample size. The role of surface atoms is widely utilized in catalysis. It is currently not easy to experimentally identify the effects of the changes in dimensionality on the magnetic properties of low-dimensional samples [15].

1.2.1 SINGLE DOMAIN PARTICLES

The domain structure changes from multi-domain to single-domain as the nanoparticles' size decrease due to a competition between magnetostatic energy and the domain-wall energy. Therefore, there is a critical volume of a particle where a multi-domain configuration is no longer stable below, and it takes more energy to create a domain-wall than to support the external magnetostatic energy of the single uniformly magnetized domain where all the spins are aligned in the same direction [11]. For single-domain nanoparticles, the magnetization process takes place by a spin rotation only. The critical diameter D_c of the single-domain nanoparticle, is reached when the magnetostatic

energy (E_{MS}) equals the domain-wall energy (E_{DW}), $E_{MS} = E_{DW}$. At the D_c the coercivity reaches its maximum. The position of this maximum depends on the material contributions from different anisotropy energy terms. The D_c typically lies in the range from *10* to *100* nanometers. In the case of a strong anisotropy, the critical diameter can be expressed as a function of the magnetic parameters of the nanoparticle by the following equation

$$D_C = 36\sqrt{\frac{\pi^2 J S^2 K_u}{a\mu_0 M_S^2}}. \tag{29}$$

where K_u is the volumetric or bulk anisotropy of the nanoparticle, J is the exchange interaction constant, a denotes the lattice constant, S is the spin, μ_0 is the permeability of the free space ($1.26{\cdot}10^{6}$ $JA^{-2}m^{-1}$), and M_S is the magnitude of the saturation magnetization. Typical values of D_c for some important magnetic materials are shown in Table I [11,16-18]. The big differences in the values seen in the Table are due to the fact that they are experimentally determined, and that magnetic properties at nanoscale are strongly dependent on the production procedure, shape, size of nanoparticles, and also size distribution of the samples. In the case of magnetic materials characterized by weak anisotropy, the critical dimension of the nanoparticles D_c is given by the solution to the following equation

$$\frac{{D_C}^2}{18}(\mu_0 M_S^2) = \frac{J}{a}\left[ln\frac{D_C}{a} - 1\right]. \tag{30}$$

A departure from sphericity of single-domain nanoparticles, assumed in Eqs. 29 and 30 for critical dimensions, has an influence on the coercivity and because of that also an

Materials	K_u [10^7erg cm^{-3}]	M_S [emu cm^{-3}]	T_c [K]	D_c [nm]	D_{SPM} [nm]
bcc-Fe	-	1745.9	1044	8.3-15	8-20
fcc-Co	0.45	1460.5	1388	7-60	3.8-20
hcp-Co	0.27	1435.9	1360	15-68	-
fcc-Ni	-	522.2	627	55-60	30-34
$L1_0$-MnAl	1.7	560	650	710	10.2
$L1_0$-FePt	6.6-10	1140	750	340	5.6-6.6
$L1_0$-FePd	1.8	1100	760	200	10
FeCo	-	1910	-	100	15-20
Fe_3Co	-	1993	-	-	20
$L1_2$-Co_3Pt	2.0	1100	-	210	9/6
$L1_0$-CoPt	4.9	800	40	610	4-7.2
$SmCo_5$	11-20	910	1000	710-960	4.4-5.4
γ -Fe_2O_3	-	380	-	60	30-40
Fe_3O_4	-	415	-	128	25-30
$CoFe_2O_4$	-	-	-	-	10
$Nd_2Fe_{14}B$	-	-	-	214	3.4

Table I. Magnetic parameters and critical diameters for different materials.

influence on the values of the critical diameter [11]. From Table II we can see that coercivity increases with increasing aspect ratio defined as the ratio of the length/width (*c/a*) of the nanoparticle.

There are also pseudo single-domain (PSD) nanoparticles that exhibit, at the vicinity of

Aspect Ratio, c/a	H_c [Oe]
1.1	820
1.5	3 300
2	5 200
5	9 000
10	10 100

Table II. The difference between the shapes of Fe nanoparticles and their respective coercivities.

critical dimensions, a mixture of single-domain (SD) and multi-domain (MD) behavior, showing a region of large and small coercivity values, respectively. When the diameter of magnetic nanoparticle drops further down below the value of D_c, the coercivity $\vec{H}_c$ starts to drop gradually from its maximum value to zero. This is where a second major finite-sized effect called superparamagnetic (SPM) behavior occurs.

The full domain theory and critical sizes diameters of the nanoparticles are summarized in Fig. 2. As we can see the curve maximizes at the D_c and rapidly drops when the diameter decreases, or slowly decays if the diameter increases.

1.2.2 SUPERPARAMAGNETISM

The superparamagnetic (SPM) behavior begins at diameter $D = D_{SPM}$ and it is marked by a strong competition between the thermal fluctuations of magnetization k_BT and the uniaxial magnetocrystalline anisotropy energy K_uV (V is the volume of nanoparticle). The higher the anisotropy K_u, the smaller the critical diameter D_{SPM},

$$D_{SPM} = \left(48\frac{k_BT}{K_u}\right)^{1/3}. \quad (31)$$

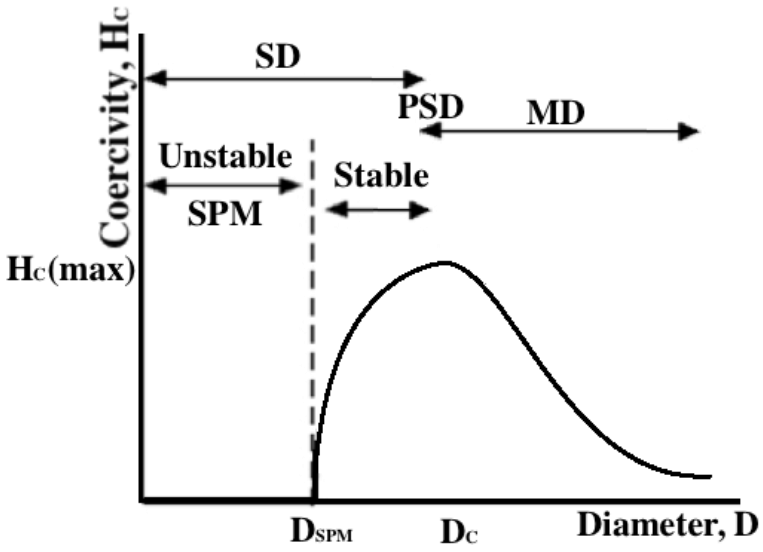

Figure 2. Coercivity as a function of magnetic nanoparticle diameter (SD – single-domain, SPM – superparamagnetism, PSD – pseudo-single domain, MD – multi-domain).

The anisotropy energy tends to keep the magnetization in a particular crystallographic direction called easy direction or easy axis [19]. The easy direction dictates where the magnetization will be spontaneously pointing at in the absence of an external field. The direction is mainly determined by an anisotropy constant K_u intrinsic to the material. The magnetic anisotropy energy, per well-isolated single-domain nanoparticle, is responsible for holding the magnetic moments along certain direction [11], can be expressed as

$$E(\theta) = (K_u V)\, sin^2\, \theta. \tag{32}$$

where $V = 4\pi r_p^3/3$ is the nanoparticle's volume with radius r_p, K_u is the effective anisotropy constant, and θ is the angle between the magnetization and the easy axis [11].

In superparamagnetic nanoparticles, the magnetization inverts spontaneously, because of the thermal energy k_BT is comparable to the anisotropy energy that creates the energy barrier K_uV separating the two energetically equivalent easy directions of magnetization, at $\theta = 0$ (parallel) and $\theta = \pi$ (antiparallel) [11,15]. Superparamagnetic nanoparticles are uniaxial, single domain, and their magnetization may spontaneously invert its direction if its temperature T is above a certain blocking temperature T_B, when the thermal energy k_BT exceeds the energy barrier K_uV. Above T_B, the system behaves like a paramagnet instead of atomic magnetic moments, and there is now a giant moment inside each nanoparticle. Such a system has no hysteresis. The direction of the magnetization fluctuates randomly. The magnetization fluctuations are defined by a frequency f or a characteristic relaxation time, $\tau^{-1} = 2\pi f$. The relaxation time of the moment of a nanoparticle, τ, is given by the Neel-Brown expression,

$$\tau = \tau_0 e^{\frac{K_u V}{k_B T}}, \tag{33}$$

k_B is the Boltzmann's constant, and τ_0 is the inverse attempt frequency (attempt time) that depends on temperature, saturation magnetization, or applied field. For simplicity the relaxation time of the moment of a nanoparticle is often assumed to be constant with a value within the range 10^{-9}-10^{-13}s [18]. The fluctuations slow down (τ increases) as the sample is cooled to with decreasing temperatures and the system appears static when τ becomes much longer than the experimental measuring time τ_m [11]. Table III summarizes some characteristic values of τ_m [18]. If the time τ_m is shorter than the relaxation time, the magnetization will appear as "blocked" (not able to move), where an

"unblocked" magnetization is typical to a nanoparticle in a superparamagnetic regime (see, Fig.2).

Techniques	Measurement Time τ_m[s]
DC Susceptibility	60-100
AC Susceptibility	10^2-10^4 (low frequency experiment) 10^{-1}-10^{-5} (classical experiment)
Mössbauer Spectroscopy	10^{-7}-10^{-9}
Ferromagnetic Resonance	10^{-9}
Neutron Diffraction	10^{-8}-10^{-12}
Magnetometer	100

Table III. Measurement time for different magnetic measurement techniques.

The temperature, which separates superparamagnetic and the "blocked" regime, is the so-called, already mentioned, blocking temperature, T_B. Below T_B the nanoparticle moments appear frozen on the time scale of the measurement, τ_m. This is the case, when $\tau_m = \tau$. The blocking temperature depends on the effective anisotropy constant, the size of the particles, the applied magnetic field, and the experimental measuring time [11]:

$$T_B = \frac{K_u V}{k_B \, ln\frac{\tau_m}{\tau_0}} . \qquad (34)$$

As an example, the experimental measuring time for a magnetometer is $T_B = (K_u V)/30k_B$. The distribution of the nanoparticle sizes results in a blocking temperature distribution. The anisotropy K_u increases with decreasing particle size, which can be seen in Table IV for samples of Fe nanoparticles with different diameter D.

D [nm]	D_c [nm]	H_c [Oe]	K_u [MJ/m^3]	D_{SPM} [nm]	T_B [K]
22	17	210	0.18	3.8	113
30	22	178	0.16	4.8	124
17	25	250	0.21	5.9	121
25	30	200	0.17	7.9	130

Table IV. Magnetic characteristics of various Fe samples derived from magnetic measurements and modeling, [20].

If the blocking temperature is determined using a technique with a shorter time window, such as ferromagnetic resonance, which has a $\tau_m = 10^{-9}$ *s*, a larger value of T_B is obtained then the value obtained from dc magnetization measurements. While in the first case the assembly of the magnetism of the nanoparticle is stable, the second case assembly of the nanoparticles has no hysteresis and is superparamagnetic. Moreover, a factor of two in nanoparticle diameter can change the reversal time from *100 yrs* to *100 ns* [11].

Thermoremanent magnetization is a magnetization-type acquired during cooling (see, Fig. 3) from temperature above the Curie temperature T_c (paramagnetic phase) to T_0 (blocked stable ferromagnetic phase) crossing the blocking temperature T_B [21]. Just above the blocking temperature T_B, the energy barrier E_B is small, and a weak-field can produce a net alignment of nanoparticle moments parallel to the external field. On cooling below T_B, the energy barrier becomes so large that the net alignment is preserved.

1.3 HEATING MECHANISMS

Heat released by magnetic substances, in an external alternating magnetic field, is related to several mechanisms of magnetization reversal and eddy currents [22].

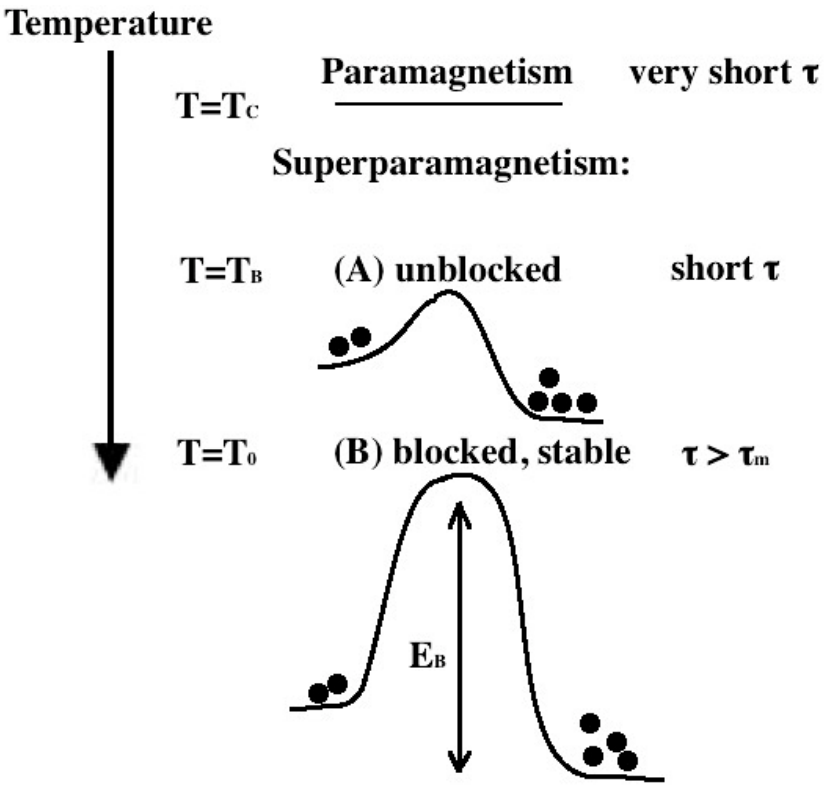

Figure 3. Thermoremanent magnetization.

The most common method to compare samples with each other is to calculate specific loss power (SLP), in units of watts per gram.

$$SLP = c\frac{\Delta T}{\Delta t}, \tag{35}$$

where the specific heat capacity is denoted by c, ΔT is the change in temperature and Δt is the change in time. Processes of magnetization reversal can be divided into two groups: reversal of the magnetization inside the particle (hysteretic losses and Neel relaxation) or the rotation of the particle in a fluid suspension (friction losses in viscous fluid and Brown relaxation). In multi-domain, the nanoparticles magnetic domain wall motion

dominates and the heat generation can be described through the hysteresis losses. However, as the diameter of nanoparticles decreases and they become single-domain, a homogeneous rotation of the magnetization occurs and the relaxation processes begin to dominate heat generation [23]. All of the mentioned above mechanisms of transforming energy, from the ac alternating magnetic field, into heat energy are summarized in four following sections.

1.3.1 HYSTERETIC LOSSES

Properties of ferromagnetic materials, above the critical nanoparticle size, D_{SPM}, are characterized by hysteresis curves (loops). The hysteresis loops above D_C are due to domain walls movement when the material is placed in a magnetic field. Depending on the alignment of the domains, with respect to the externally applied magnetic field, they grow or shrink, which makes the material more and more magnetized in the field direction [24,25] (see Fig. 4). When the external field changes direction, first the demagnetization occurs followed by a magnetization in a new direction. The movement of the domain walls through the crystal lattice, during the repeated magnetization and demagnetization processes, results in energy losses referred to as the hysteretic losses. The frequency of the magnetization and demagnetization processes depends on frequency f of the externally applied field.

The hysteresis losses may be determined by integrating the area of the hysteresis loop, which represent a measure of the energy dissipated per cycle of the magnetization reversal [22]. The corresponding power loss is:

$$P = \mu_0 f \oint H dM. \tag{36}$$

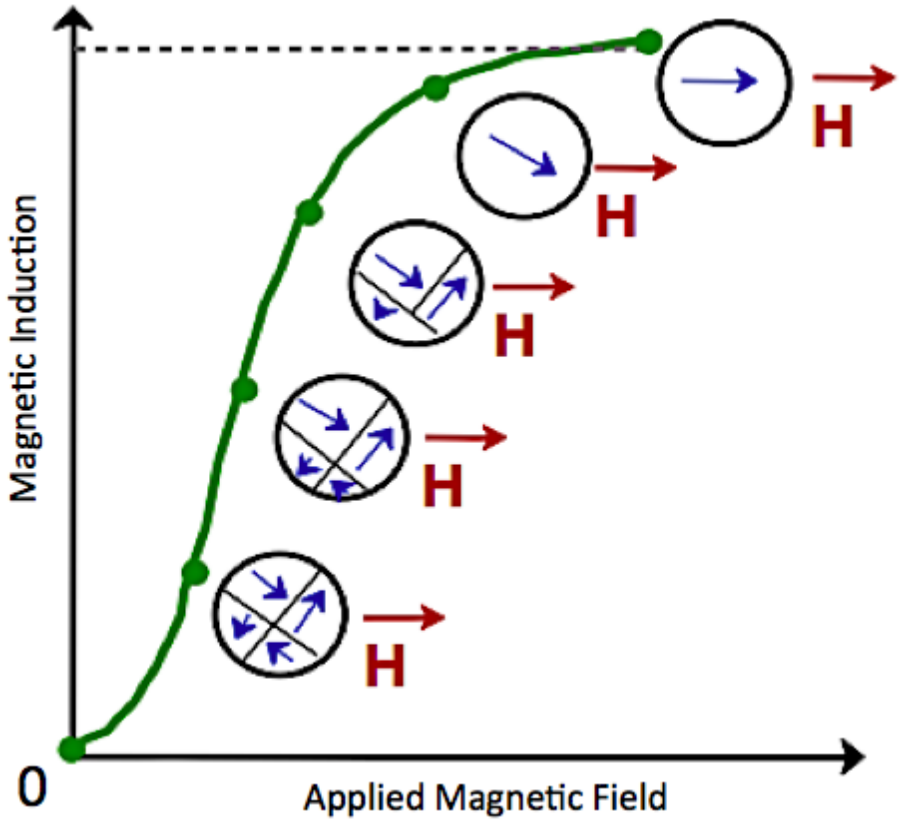

Figure 4. Magnetic induction as a function of applied magnetic field with domain walls dynamics (virgin magnetization curve) [26,27].

1.3.2 VISCOUS LOSSES

The generation of heat, as a result of the viscous friction between rotating nanoparticles and surrounding medium is called the Brown mechanism [22]. This type of loss is significant but not restricted only to superparamagnetic nanoparticles. In general, nanoparticles, which may be regarded as small permanent magnets with a remanent magnetization M_R, are subject to a torque moment $\tau = \mu_0 M_R H V$, when exposed to a rotating magnetic field H [22]. In the steady state, the viscous drag in the liquid

($12\pi\eta Vf$), where V is volume of the particles and η is a viscosity of the surrounding, is counteracted by the magnetic torque τ. The loss energy per cycle is simply given by $2\pi\tau$ [28].

1.3.3 NEEL AND BROWN RELAXATION

With decreasing nanoparticle size the energy barrier for the magnetization reversal decreases [22] and eventually a transition of the nanoparticle from multi-domain to single domain occurs. Consequently, the thermal fluctuations have an increasing impact on the heat losses due to the relaxation processes. The relaxation processes can be observed if the measurement frequency is smaller than the characteristic relaxation frequency of the nanoparticle system. There are two characteristic relaxation frequencies: Neel and Brown. In the case of Néel relaxation τ_N, which is caused by the fluctuation of the magnetic moment direction across an anisotropy barrier, the characteristic relaxation time τ_N of a nanoparticle system is given by

$$\tau_N = \tau\,(\pi k_B T/4K_u V_M)^{1/2}, \qquad (37)$$

where the relaxation time τ of the moment of a nanoparticle is given by Eq. 33. The relaxation effects cause vanishing of the remnant magnetization and coercivity. Therefore, there are no hysteretic losses below the critical size D_{SPM} [29]. This transition to superparamagnetism occurs in a narrow frequency range. Losses in the superparamagnetic state also lead to heating of the nanoparticles. The frequency dependence of the relaxation of the nanoparticle ensemble can be given through the complex susceptibility. The imaginary part of the susceptibility $\chi''(f)$ which is related to magnetic losses, is described by

$$\chi''(f) = \frac{\chi_0 \phi}{1+\phi^2}, \tag{38}$$

where $\chi_0 = \frac{\mu_0 M_S^2 V}{k_B T}$, f is the frequency, $\phi = f\,\tau_{eff}$, and M_S is the magnitude of the saturation magnetization [2]. The power loss density P related to $\chi''(f)$ is given by

$$P = \mu_0 \chi''(f) \pi H_0^2 f, \tag{39}$$

where H_0 is the intensity of ac magnetic field. The loss power density $P\ [Wm^{-3}]$ is related to the SLP $[Wg^{-1}]$ by the mean mass density of the nanoparticles. At low frequencies, $\phi << 1$, in the superparamagnetic regime, the losses increase with the square of frequency, while for $\phi >> 1$ the losses saturate at $P = \mu_0 M_S^2 V/\tau_N$ and become independent of frequency. At the transition between those two regimes, the spectrum of the imaginary part of the susceptibility has a peak dependency on the mean nanoparticle size through τ_N. The very strong size dependence of the relaxation time leads to a very sharp maximum of the loss power density [22,29]. Therefore, the highest heating power output can only be achieved through careful adjustment of field parameters (frequency f and amplitude H) in accordance with the nanoparticle properties (size and anisotropy) [29]. Accordingly, the homogeneity of the nanoparticle ensemble has a very high importance. In a fluid suspension of magnetic nanoparticles, which are characterized by a viscosity η, a second relaxation mechanism occurs due to reorientation of the whole nanoparticle. This is commonly referred to as Brown relaxation τ_B. Brown relaxation expressed with the characteristic relaxation time for spherical nanoparticles can be written as

$$\tau_B = \frac{4\pi\eta r_h^3}{k_B T}, \tag{40}$$

where $r_h=r_p+\delta_c$ is the hydrodynamic radius, which is equal to the radius of the magnetic nanoparticle core r_p and the thickness of coatings of the particle δ_c (e.g., biocompatible layer) [22]. This effect becomes essential if the magnetic moment direction is strongly coupled to nanoparticles itself, for instance, by a large value of the magnetic anisotropy combined with easy rotation of the particle due to low viscosity [29]. The power loss density is given by Eqs. 38 and 39, but using $\phi = f\,\tau_B$. The dependence of the power loss density on size, in the case of Brown relaxation, is different from the case of Neel relaxation. It increases monotonously with the size of the nanoparticle up to a saturation value for $\phi >> 1$ [29]. The faster of the relaxation mechanisms is dominant and an effective relaxation time may be defined by

$$\tau_{eff} = \frac{\tau_N \tau_B}{\tau_N + \tau_B}, \tag{41}$$

where $\phi = f\,\tau_{eff}$ for the power loss density.

1.3.4 EDDY CURRENTS

An alternating magnetic field induces eddy currents as a consequence of the law of induction. Heating induced by eddy currents is negligible in comparison to the purely magnetic heating generated by the magnetic particles since the heating power decreases with decreasing diameter of the conducting material.

1.4 HEAT TRANSFER MODEL

Depending on application there are different requirements for thermal properties of the magnetic nanoparticles. The main application that is referred to while analyzing and qualifying the magnetic nanoparticles under investigation, described in Section 2.1, is the application for hyperthermia treatment. This application was the reason to study the heat

transfer in biological tissue. In the following sections hyperthermia as a cancer treatment will be briefly introduced, secondly limitations introduced by hyperthermia on the external magnetic field power and the magnetic nanoparticles will be discussed, and at last the mathematical model of heat transfer will be presented.

1.4.1 MAGNETIC HYPERTHERMIA

The healing power of heat has been known for a very long time and used to cure very different diseases. It is today also recognized as a cancer therapy. The first reports of heat being useful in cancer treatment are from the years 1866-67 by Wilhelm Busch and William Coley who noted the disappearance of a sarcoma after high fever caused by the immune systems response to an bacterial infection [30]. It was already then concluded that the growth of cancerous cells stops in temperatures above approximately *42°C*, whereas healthy cells can tolerate even higher temperatures [29]. Cancer treatment at temperatures from *42°C* to *45°C* (varies in the literature) is referred to as a hyperthermia. Temperatures higher than *44°C* are controversial because the amount of side effects increases very rapidly. However, higher temperature than *44°C* is tolerable by the human body if they occur locally. Therefore, for an increased effectiveness of hyperthermia, it is desired to, instead of full body treatment, achieve targeting possibility to treat only tumor-affected areas. Such an improvement was brought by the magnetic nanoparticles suspended in a fluid. The magnetic suspension can be injected into tumor tissue and, in an external alternating magnetic field, the heat generated by the magnetic nanoparticles concentrates mainly on the tumor. Jordan in 2001 [31] and Gneveckow in 2005 [32] reported the initiation of the first clinical trials. MacForce Technology [33] is currently leading technology in clinical trials of thermotherapy with magnetic nanoparticles. In

2011 Jordan and Maier-Hauff [34] have reported promising results of using magnetic nanoparticles in conjunction with a low radiation dose. They concluded the method as safe and effective in the treatment of recurrent glioblastoma (the most common and most aggressive brain tumor in humans). Most commonly used magnetic nanoparticles for hyperthermia treatment are iron oxide nanoparticles because of their low toxicity. The primary problem in human studies is to deliver the magnetic-nanoparticle suspension to the tumor. This can be achieved in two main ways, which are both difficult to control: by injecting the nanoparticle suspension directly into the tumor or into blood vessels that supply the tumor, or by using a targeted delivery to the tumor, either by labeling the magnetic nanoparticles with tumor-specific antibodies or by nanoparticle guidance using inhomogeneous magnetic fields [29].

1.4.2 EXTERNAL FIELD POWER

Except of the heat generated by nanoparticles, summarized in Section 1.3, during hyperthermia treatment there are additional eddy currents induced in the tissue, both cancerous and healthy. The specific electrical conductivity of tissue is much lower than that of metals, however, the region exposed may be large, and for this reason Brezovich in 1988 [29] came up with a critical heat power, based on a whole-body treatments. The Brezovich critical power $(H \bullet f)_{crit} = 4.85 \cdot 10^8\ A/(m \bullet s)$ is a product of the frequency f of the applied external field and the magnitude of the magnetic field H. This critical power defines the maximum product of those two quantities that is safe compared to cause overheating of patients [32]. Therefore, for hyperthermia treatments the specific loss power (SLP) as an increasing function of frequency f and field amplitude H is limited [35]. This is the reason why ongoing research tries to find materials with very high SLP.

1.4.3 MAGNETIC NANOPARTICLES

Application of the magnetic nanoparticles in hyperthermia should go through the optimization of mean nanoparticles' diameter, and its size distribution towards larger SLP values [22]. Fig. 5 shows the experimentally determined dependence of SLP on mean nanoparticle diameter for different superparamagnetic iron oxide nanoparticles [29]. There is a rapid increase in SLP with increasing diameter, and it is clear that for multi-domain nanoparticles this trend should be reversed. Therefore, a maximum SLP for nanoparticles between multi-domain and superparamagnetic size range is expected, though the position and height of that maximum are currently unclear [29].

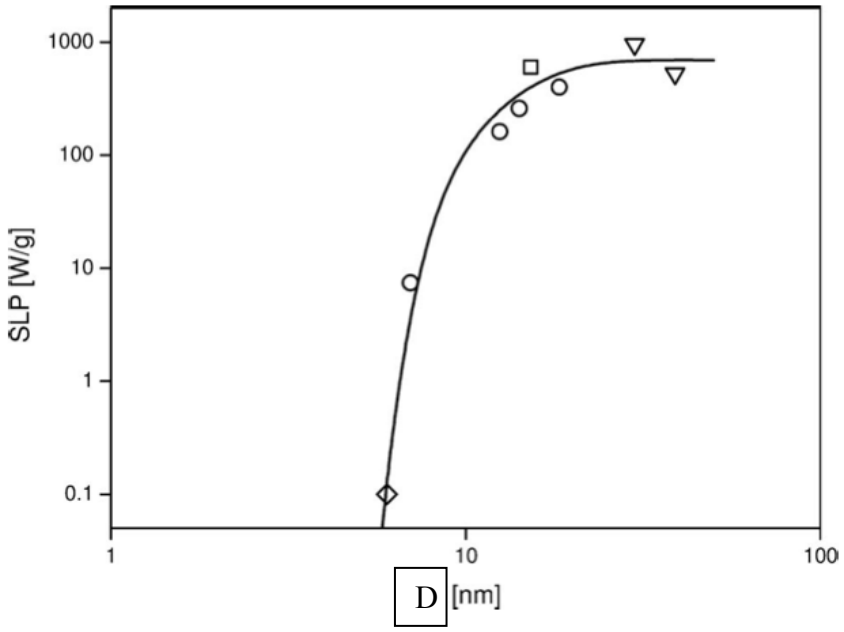

Figure 5. Specific loss power (*400 kHz, 10 kA/m*) depending upon mean nanoparticle core diameter for iron oxide magnetic nanoparticles [29].

Different materials are being explored as candidates with higher SPL to substitute

iron oxide (magnetite Fe_3O_4), which are currently the most used in research and clinical trials. Iron and cobalt nanoparticles investigated in this study (see, Section 2.1) are expected to show an enhancement of the magnetic moment per particle comparing to iron oxide nanoparticles, because of higher saturation magnetization (see, Section 3.1.3). This means that a fewer nanoparticles suspended in a fluid could be used during treatment, provided that Fe and Co nanoparticles are biocompatible. Biocompatibility of nanoparticles for hyperthermia treatment means: a chemical stability in the bio-environment, appropriate circulation time in blood, harmless biodegradability, nontoxicity, and a preference of agglomeration in tumor cells than in healthy cells, etc., [28,29]. Based on considerations in Section 1.2, a maximum of SLP for nanoparticles between multi-domain and superparamagnetic size range is expected. In addition to mean nanoparticle diameter, the nanoparticle size distribution has also a major effect on SLP value in such a way that a narrow-normal distribution gives higher SLP than a log-normal distribution [29]. Additionally, the effective magnetic anisotropy and the coating of the magnetic nanoparticles are also important for Neel and Brown relaxation losses, respectively. The above discussion demonstrates that a good knowledge of the structural and magnetic properties of magnetic nanoparticles is a compulsory precondition for designing valuable nanoparticle suspensions with large SLP for the hyperthermia application.

1.4.4 HEAT MODEL

The demand of specific heating power of the magnetic nanoparticles for hyperthermia is determined first by the temperature elevation needed to damage the cancer cells, and then by the concentration of magnetic nanoparticles in the tissue

selected for therapy [29]. The therapeutically useful elevations of the body temperatures are of the order of few degrees.

The temperature elevation in the tumor during the hyperthermia treatment is a result of the balance of the two competing processes of heat generation within the magnetic nanoparticles and heat depletion into surrounding tissue mainly due to heat conduction [32]. After injecting the magnetic suspension into the tumor, the nanoparticle distribution must be monitored with suitable diagnostic means, like for example MRI [29] and for a given specific power of the magnetic material, a temperature increase may be estimated by solving so called bio-heat equation [35]. A small tumor surrounded by the normal tissue was modeled as a sphere of the radius R. We assume that the magnetic nanoparticles are injected into, and homogenously distributed in the tumor. Therefore, the tumor can be treated as a spherical heat source of constant power density P excited by an alternating magnetic field [36]. Heat is then symmetrically transfered in the radial direction. The temperature distribution in the tumor and normal tissues is the function of distance r from the center of the sphere and time t. The heat transport in the tumor ($0 \le r \le R$) and in normal tissue ($R \le r \le a$) with constant physiological parameters is expressed in the following equations [35]

$$\rho_1 c_1 \frac{\partial T_1}{\partial t} = k_1 \frac{1}{r^2}\frac{\partial}{\partial r}\left(r^2 \frac{\partial T_1}{\partial r}\right) + w_{b1}\rho_b c_b (T_b - T_1) + q_{m1} + P \text{ for } 0 \le r \le R, \qquad (42)$$

$$\rho_2 c_2 \frac{\partial T_2}{\partial t} = k_2 \frac{1}{r^2}\frac{\partial}{\partial r}\left(r^2 \frac{\partial T_2}{\partial r}\right) + w_{b2}\rho_b c_b (T_b - T_2) + q_{m2} \text{ for } R \le r \le a, \qquad (43)$$

where ρ, c, k, and T denote density, specific heat, thermal conductivity, and temperature in two regions, respectively. ρ_b, c_b, and w_b are respectively density, specific heat, and

perfusion rate of blood, q_m is the metabolic heat generation, T_b is the arterial temperature specified as 37°C. The region $0 \leq r \leq R$ is a composite of tumor and magnetic nanoparticles. The effective density ρ_1 and the effective specific heat c_1 are calculated as $\rho_1 = \psi\rho_M + (1-\psi)\rho_T$ and $c_1 = \psi c_M + (1-\psi)c_T$, where subscripts M and T symbolize the magnetic nanoparticles and the tumor tissue. ψ is the volume fraction of magnetic nanoparticles [35]. An extension of this model leads to an equation for the power [42]

$$P = (\mu_0 \pi f H_0 M_S \psi)\left[\coth\left(\frac{\mu_0 H_0 M_S V}{k_B T_1}\right) - \frac{k_B T_1}{\mu_0 H_0 M_S V}\right]\left[\frac{2\pi f \tau_{eff}}{1+(2\pi f \tau_{eff})^2}\right], \quad (44)$$

where $V = 4\pi r_p^3/3$ is the volume of the nanoparticle, and τ_{eff} is given by Eq. 41.

2. MATERIALS, METHODS, AND PROCEDURES

2.1 SAMPLES

Samples with different mean diameters of iron nanoparticles and cobalt nanoparticles were prepared in Cambridge University, United Kingdom by group supervised by Andrew Wheatley [1].

2.1.1 SAMPLE PREPARATION

Reactions to create the magnetic nanoparticles were carried out under an argon atmosphere using standard air sensitive techniques. Details of the synthesis procedures and the schemes for both the iron and cobalt nanoparticles are presented in the two following Sections.

2.1.1.1 IRON

Iron nanoparticles were synthesized by thermal decomposition of iron pentacarbonyl ($Fe(CO)_5$) in the presence of OA/OE or PVP (Scheme 1). Solutions of $Fe(CO)_5$ were injected into mixtures of a capping agent at 100°C and the mixtures were heated to reflux [1]. Reflux is a distillation technique based on the condensation of vapors and the return of this condensate to the system [40]. Surfactant concentration and reflux time were adjusted in order to obtain nanoparticles of a specific size. The reaction mixture was cooled to room temperature and Fe nanoparticles were separated by the addition of ethanol followed by centrifugation. Lastly, re-dispersion happened in an organic solvent and the powder of nanoparticles was created.

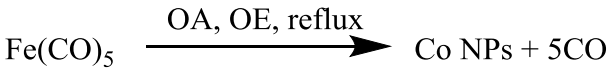

Scheme 1: Fe nanoparticle formation (OA = oleic acid, OE = octyl ether)

2.1.1.2 COBALT

Cobalt nanoparticles were synthesized by the thermal decomposition [1] of dicobalt octacarbonyl ($Co_2(CO)_8$), triscobalt nona(carbonyl)chloride ($Co_3(CO)_9Cl$), or tetracaobalt dodecacarbonyl ($Co_4(CO)_{12}$) in the presence of either trioctylphosphine oxide(TOPO)/OA, TPP/OA, PVP, or NaAOT (Scheme 2) [1]. The cobalt source was introduced as a solid or in solution to refluxing capping agent. The concentrations of the reagents and the reflux times were adjusted in order to obtain nanoparticles of a specific size. The reaction mixture was cooled to room temperature and Co nanoparticles separated, re-dispersed and finally prepared in a powder form as for Fe.

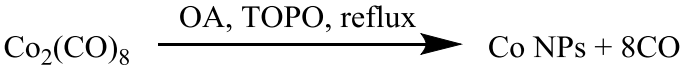

Scheme 2: Co nanoparticle formation (OA = oleic acid, TOPO = trioctylphoshine oxide)

2.1.2 CHARACTERIZATION OF SAMPLES

The nanoparticles were characterized, by collaborators from Cambridge, using a JEOL JEM-3011 HRTEM (high-resolution Transmission Electron Microscopy) at nominal magnifications of x100k to x800k [1]. The particle sizes were analyzed using the program Macnification 2.0.1 at Cambridge by counting the diameters of *100* particles in lower magnification images, defining size intervals of *0.2 nm* between $d_{min} \leq d \leq d_{max}$ and counting the number of particles falling into these intervals, the data was then used to construct particle size distributions using DataGraph 3.0 [1].

Masses of the samples were measured with a mass balance Tare FE Series Model 100A, with precision to the nearest tenth of a thousand gram (*0.0001 g*). The balance is shielded from all sides, which protects samples from environment during the measurement. The method used for measuring a mass of a sample was to first measure the mass of a glass tube m_{gt} which is used as a sample container, which is to be mounted inside the coil for the heat generation measurements. After the measurement of the glass, a sample of nanoparticles, spherical in shape, is inserted carefully into the tube and their overall mass m_{gt+s} is measured. To get a mass of the sample those two masses are subtracted $m_s = m_{gt+s} - m_{gt}$.

2.1.3 MATERIALS SUMMARY

Short summary of iron and cobalt nanoparticles is presented in the following Sections.

2.1.3.1 IRON

Iron is a common element on Earth since it forms most of the outer and inner core of our planet. It oxidizes easily creating compounds like iron (II) oxide or iron (III) oxide. Iron has a high mass saturation magnetization in the bulk form at room temperature, $\sigma_S(Fe) = 218\ Am^2kg^{-1}$ [1]. Iron nanoparticles with measured averaged diameters are summarized in Table V.

2.1.3.2 COBALT

Cobalt can only be found in the Earth's crust. Cobalt has, similar to iron, a high mass saturation magnetization in bulk form at room temperature, $\sigma_S(Co) = 161\ Am^2kg^{-1}$ [1]. The averaged sizes of measured cobalt nanoparticles are summarized in Table VI.

Additionally, iron and cobalt's heat capacity are compared in Table VII. As we can see iron has higher heat capacity.

Nanoparticle	D [nm]
BKFe7	5.60 ± 0.48
BKFe10	7.97 ± 1.52
BKFe15	10.31 ± 1.83
BKFe6	11.25 ± 1.40
BKFe20	18.31 ± 1.95
BKFe25	18.61 ± 1.97
BKFe5	20.00 ± 1.27
PTFe2	21.44 ±1.73
PTFe03	12.61 ± 1.62

Table V. Averaged sizes of measured iron nanoparticles [36].

Name	D [nm]
BKCo31	6.51 ± 0.59
BKCo51	7.31 ± 0.78
BKCo41	8.21 ± 0.104
BKCo1	8.66 ± 1.22
PACo8	8.84 ± 1.26
PACo9	9.23 ± 0.65
PACo2	10.19 ± 1.08
PACo1	17.1 ± 3.33
BKCo21	19.42 ± 4.45

Table VI. Averaged sizes of measured cobalt nanoparticles [36].

Nanoparticle	Heat capacity at 293K [J/$^{\circ}$Cg]
Co	0.4198
Fe	0.4504

Table VII. Heat capacity for Co and Fe nanoparticle.

2.1.3.3 IRON AND COBALT COMPARED TO IRON OXIDE

The mass saturation magnetization of the samples of iron and cobalt nanoparticles [1,41] are gathered in Table VIII together with value for iron oxide. From this comparison we can see that iron has the highest saturation magnetization and iron oxide the lowest saturation magnetization. Therefore, iron nanoparticles are expected to produce the highest power in an ac magnetic field.

Material	σ_S [Am^2kg^{-1}]
Fe	218
Co	161
Fe_3O_4	90-92

Table VIII. Mass saturation magnetization for iron, cobalt and iron oxide.

2.2 HEAT MEASUREMENT EQUIPMENT AND SETTINGS

The system used in this project to measure the heating rate of the magnetic nanoparticles, when irradiated by the magnetic field, consists of a function generator, a current supply, a power supply, a chiller, a coil, a temperature probe, and a vacuum pump connected together as shown in Figs. 6 and 7. The custom-made power supply is capable of producing an alternating current at the range of kilohertz. The produced alternating current is fed to the coil. Measurements were done using a frequency of $f = 174$ *kHz* for the current of $I = 15$ *A*. This frequency generates the magnetic field of $B = 20.6\ \mu T$ inside the coil [9]. Those values were in agreement with the hyperthermia treatment requirements because the product of the magnetic field amplitude H and the frequency f, $H \bullet f = 2.85 \cdot 10^6$ *A/(m•s)* is much below the critical limit of $4.85 \cdot 10^8$ *A/(m•s)*.

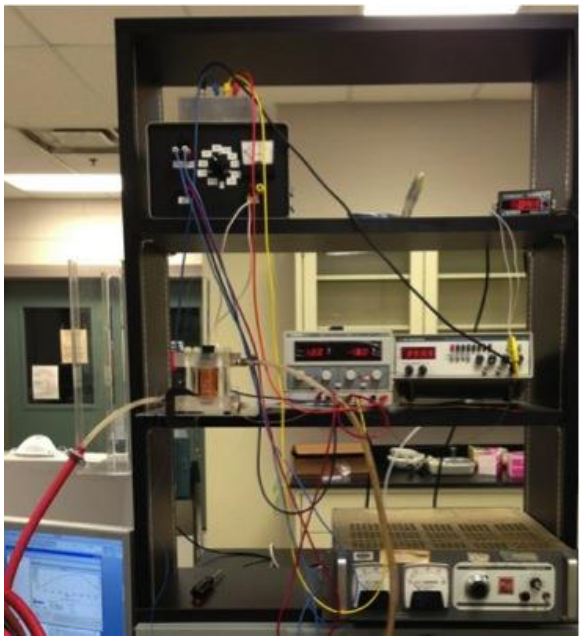

Figure 6. Magnetic heating system.

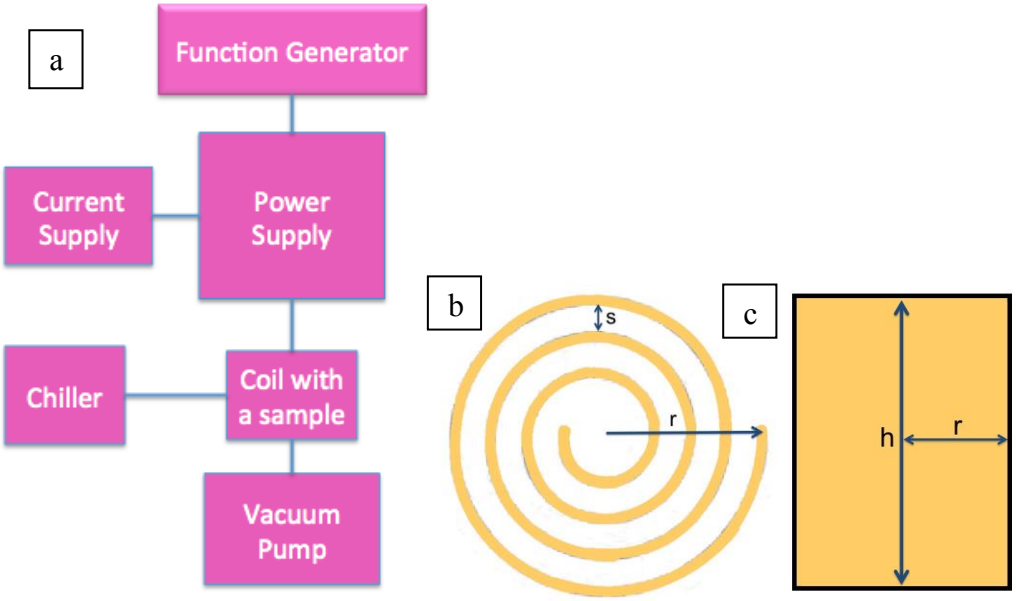

Figure 7**.** Schematic of the magnetic heating system (a), top (b), and side (c) view of the coil.

The function generator, BK Precision 4011A which was used to achieve the *f = 174 kHz* had to be set on *348 kHz* to feed the power supply. The doubling of the frequency is due to the way the power supply is designed. The coil used has a diameter of *3 cm*, a length of *4 cm*, was also custom made and consists of insulated copper sheets wrapped around each other *20* times in the form of a spiral solenoid. The water chiller cools the coil externally and keeps it at constant temperature. The vacuum pump is connected to the coil enclosure to eliminate conduction and convection from the coil to the nanoparticle sample placed inside of it. Each sample before measurement is inserted into a NMR glass tube with diameter of *4.57 mm*, which is afterwards mounted inside the coil using a rubber cork with a proper sized opening. The NMR tube together with the sample under investigation is placed in the middle of the cross section of the coil, through the opening of the cork, and also in the middle of the height of the coil. For measuring the temperature differences, a fiber-optic temperature sensor (FOT-L-SD Model) with an accuracy of *0.0001 K*, is used. The temperature measurements are based on variations of reflected light when compared to the emitted light due to the thermal expansion of the glass used within the sensor. The thermal inertia is reduced almost to zero allowing ultrafast temperature monitoring (see, Table IX). The structure of the sensor (Fig. 8) has an influence on minimum amount of the sample needed to assure that the sensitive part of the sensor is imbedded in the sample during measurements.

All samples analyzed in this study are in the form of dry powder.

2.3 SLP' CALCULATIONS

For meaningful averaging of the results when a mass of sample is varied from trial

Temperature range	40°C to 250°C
Resolution	0.001°C
Accuracy	0.01°C
Response time	≤ 0.5s

Table IX. Specifications of the fiber optic temperature sensor FOT-L-SD model [37].

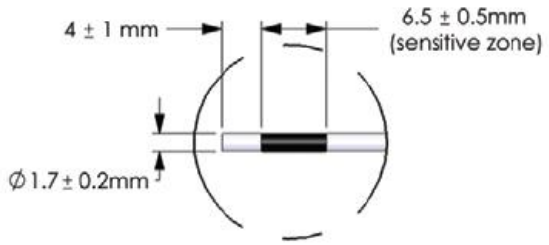

Figure 8. The fiber optic temperature sensor FOT-L-SD model [37].

to trial, SLP' should be used instead of SLP. SLP' is defined as SLP divided by the mass of a sample and expresses in units of watt per gram squared, SLP' = SLP/m_s $[W/g^2]$. First, using the heating curves, produced by the software of the temperature sensor (FOT-L-SD model) SLP is calculated. The heating curve is a plot of the temperature versus time. To get a SLP value (see Eq. 35) the gradient of a heating curve is needed which is a change in temperature in unit time $\Delta T/\Delta t$. This gradient (HR) is found by importing temperature (Temp) data to Matlab, creating time (Time) data using the frequency of acquiring data of the temperature sensor according to the following lines of code:

```
lT=length(Time);
i=0;
for a=t:lT-150
   i=i+1;
   F=polyfit(Time((1+a):(s+a)),Temp((1+a):(s+a)),1);
```

```
    yy(i)=F(1);
  end
 HR=max(yy)
```

To calculate SLP we need heat capacity of the used nanoparticles. The values of the heat capacity for iron and cobalt are gathered in Table VII. Finally, the mass m_s of the sample is needed to find SLP' for a given sample. Method of finding m_s is given in Section 2.1.2. It is advantageous for hyperthermia treatment to achieve the temperature enhancement with as low as possible amount of nanoparticles [22].

2.4 HEAT MODEL

A Matlab code based on a computational model for the hyperthermic elimination of cancerous tissues has been created in collaboration with Mathematics Department, WSU. Our model hypothesizes the deposition of magnetic nanoparticles uniformly distributed in cancerous tissue cells. The distribution can be accomplished by direct injection or circulatory delivery of those nanoparticles. The goal is to raise temperature of cancerous cells from *37°C* to approximately *45°C* (raise of about *8°C*) using an externally applied alternating magnetic field. Since growing tumors induce capillary development, we assume that nanoparticles injected in the vicinity of a tumor will be delivered to those capillaries. Due to surface modifications, it is assumed that the nanoparticles will be attached to the membrane of those blood vessels behind where the tumor cells exist. We predict the heat flow through the capillary walls and cell membranes into the diseased cell bodies. We also considered the heat loss into surrounding healthy tissue and the heat loss due to blood perfusion. All mentioned mechanisms are included in the bio-heat

equation [35] that the created Matlab code was solving. Numerical values of all parameters are taken from the paper written by Chin-Tse Lin and Kuo-Chi Liu [35]. The magnetic field amplitude and frequency are 50 mT and 300 kHz. Nanoparticles used are 19-nm magnetite nanoparticles that can dissipate the power $P = 1.95 \cdot 10^5\ W/m^3$ (is assumed to be constant). Also as a development of the model the Eq. 44 is considered instead of a constant dissipated power with following values for iron oxide:

$M_s = 446000\ A/m$, $K_u = 23000\ J/m^2$, and ranges of numbers for r_p ($3 \cdot 10^{-9}\ m - 15 \cdot 10^{-9}\ m$), δ_c ($0.2 \cdot 10^{-9}\ m - 20 \cdot 10^{-9}\ m$), f (50 kHz – 500 kHz), H_m (0 – 20000 A/m), ψ (0 – 0.001), and η (0 – 5 $kg/m \cdot s$). Initial condition of the body temperature for tumor and healthy tissue is set to $37°C$. The volume fraction of the particles is $\psi = 2 \cdot 10^{-5}$. Thermal conductivities are $k_1 = k_2 = 0.502\ W/mK$. Perfusion rates of blood are $w_{b1} = w_{b2} = 0.0064\ m^3/s/m^3$. Metabolic heat generation parameters are $q_{m1} = q_{m2} = 540\ W/m^3$. The density and specific heat capacity of healthy tissue are $\rho_2 \cdot c_2 = 1060 \cdot 3600\ J/m^3/K$. The density and specific heat capacity of blood are $\rho_b \cdot c_b = 4.18 \cdot 10^6\ J/m^3/K$. The density and specific heat capacity of the tumor are $\rho_1 = \psi\rho_M + (1-\psi)\rho_2$ and $c_1 = \psi c_M + (1-\psi)c_2$ where for a magnetite $\rho_M = 5180\ kg/m^3$ and $c_M = 670\ J/kgK$. The dimensions of the tumor and of normal tissue were regarded as $R = 5\ mm$ and $a = 15\ mm$.

3. RESULTS AND DISCUSSION

3.1 HEATING MEASUREMENTS

The measurements of the temperature changes versus time (heating curves) for the Co and Fe nanoparticles were done in a magnetic field of $B = 20.6\ \mu T$ inside the coil which oscillated at the fixed frequency of $f = 174\ kHz$. The relative permeability of the human body is approximated by the relative permeability of water which equals $\mu_r = 0.999992 \cong 1$. The product of the magnetic field $H = B/\mu_0\mu_r$ and the frequency f results in the value of $(H \bullet f)_{system} = 2.85 \bullet 10^6\ A/(m \bullet s)$. It is seen that $(H \bullet f)_{system}$ for our experimental setup is much lower than the critical value, $(H \bullet f)_{critcal} = 4.85 \cdot 10^8\ A/(m \bullet s)$, which means it can be imposed on human body under the treatment without harming it (see, Section 1.4.2). Therefore, the results acquired in this study and presented in the following sections are relevant for application to hyperthermia.

3.1.1 HEATING CURVES

All the measurements of the change in temperature were done on dry samples of magnetic nanoparticles placed in a glass tube without any fluid added. The particles were aggregated in small clusters, visible to the eye, and attempts were made to crush those clumps into fine powder as originally made.

Firstly, before placing a sample of magnetic nanoparticles in the ac magnetic field its mass was measured following procedure described in Section 2.1.2. All the mass values can be found in Appendix 1 and 2 for iron and cobalt, respectively. The masses are in the range from *0.01* to *0.18 g*, which justifies usage of the high precision balance.

Secondly, the graph of the temperature of each individual sample placed in the ac magnetic field versus time, called heating curves, has been acquired. Measurements were repeated *2* to *5* times for each sample and sometimes the mass of the sample was varied. The two initial experiments were conducted to check the repeatability of the results. The calculations of the standard deviations can be found in Appendix 1 and 2. Typical heating curves for the Fe and Co nanoparticle samples are presented in Fig. 9 and 10, respectively. As it can be seen from these figures, BKCo41 from the cobalt samples and BKFe25, BKFe20, and BKFe10 from the iron samples gave the highest temperature change. The sample PACo1 had the best result among the cobalt with diameter of *17.10 ± 3.33 nm*. The values of SLP for PACo1 can be seen in the table in Appendix 2.

All the experiments were done at a room temperature of *20°C*. The chiller has a broad range of temperatures of the water it can operate on. It was of interest to adjust the chiller to *37°C* to simulate the body temperature for checking the possible suitability of the particles under investigation in hyperthermia treatment. Unfortunately, the amount of sample used and its appropriate heat production, were not in position to overcome background temperature of *37°C*. Consequently, all data were collected at room temperature with the chiller temperature set to *20°C*. From Fig. 9, we can see that the sample BKFe25 gives the highest increase in temperature within 100 seconds for the iron nanoparticles. The change in temperature is about *12.5°C*. Second best result is observed in BKFe20 with an increase of about *11.5°C*, which is much better than in the sample BKFe15 of the same mass which gave an increase in temperature only in the order of *0.5°C*. Table X summarizes the results in Fe nanoparticles with an average diameter of

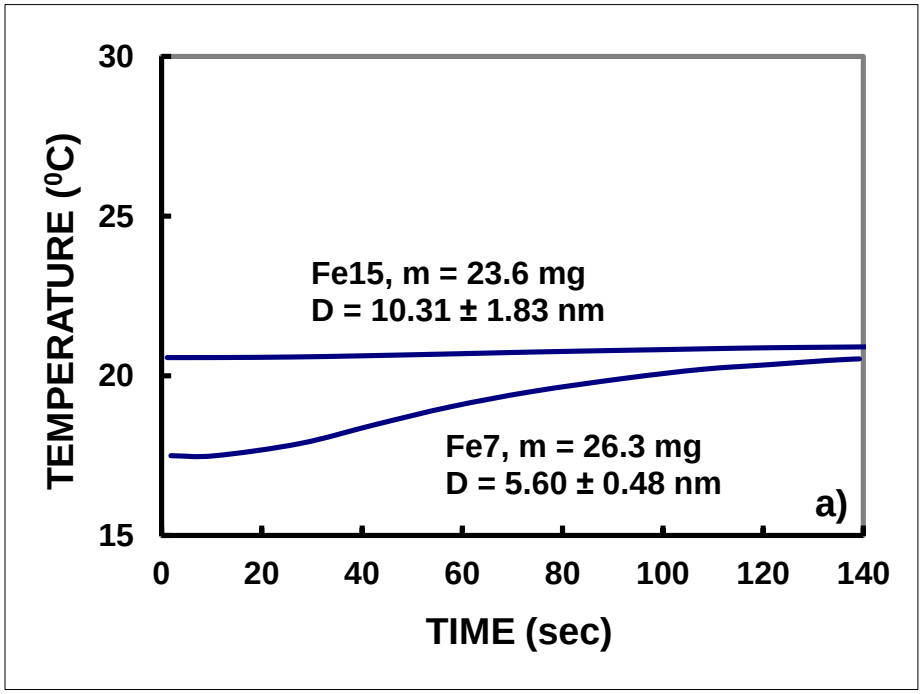
30
25
20
15
TEMPERATURE (⁰C)
Fe15, m = 23.6 mg
D = 10.31 ± 1.83 nm
Fe7, m = 26.3 mg
D = 5.60 ± 0.48 nm
a)
0
20
40
60
80
100
120
140
TIME (sec)

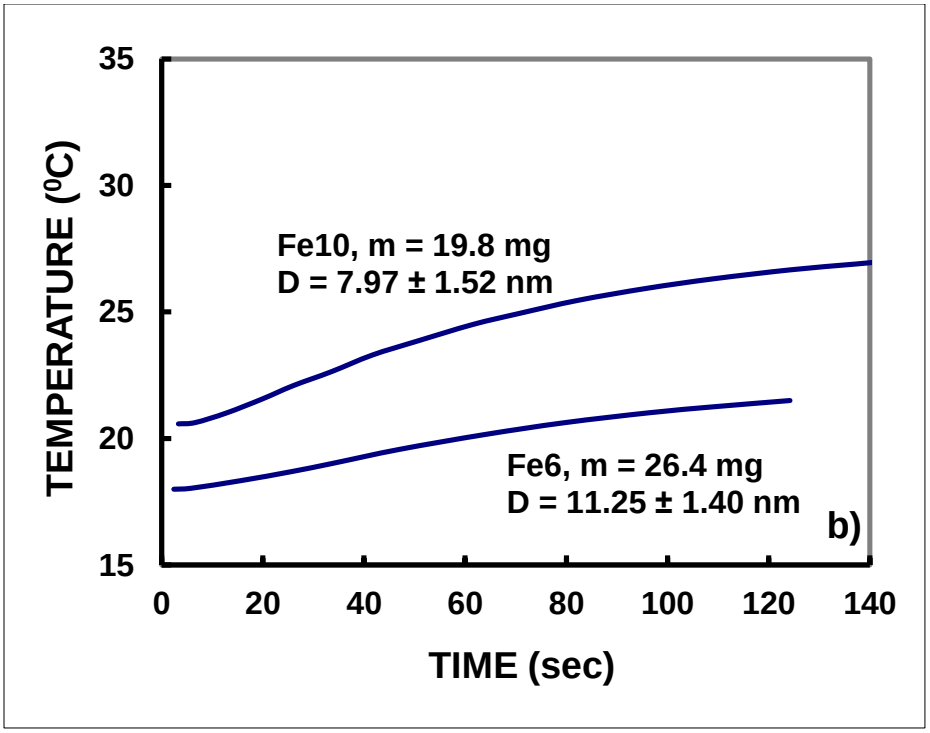
35
30
25
20
15
TEMPERATURE (⁰C)
Fe10, m = 19.8 mg
D = 7.97 ± 1.52 nm
Fe6, m = 26.4 mg
D = 11.25 ± 1.40 nm
b)
0
20
40
60
80
100
120
140
TIME (sec)

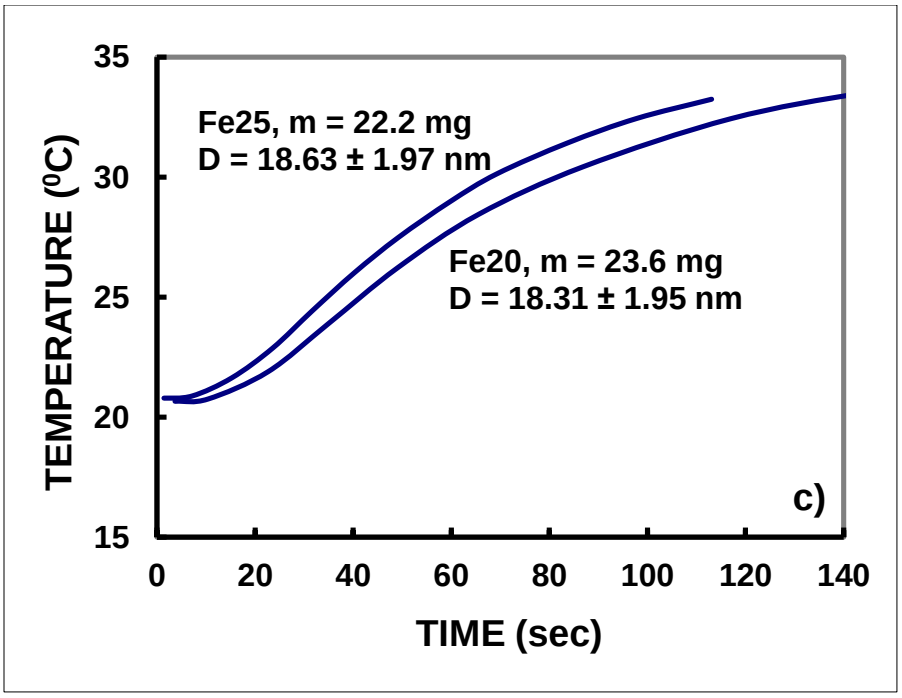

Figure 9. Heating curves for Fe magnetic nanoparticles with different diameters (BKFe –).

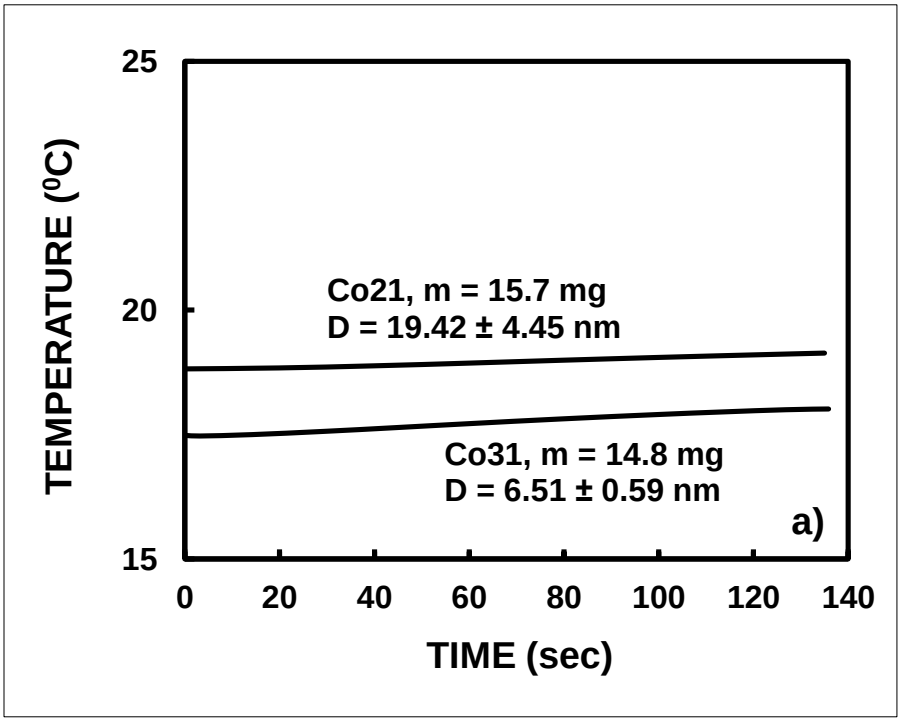

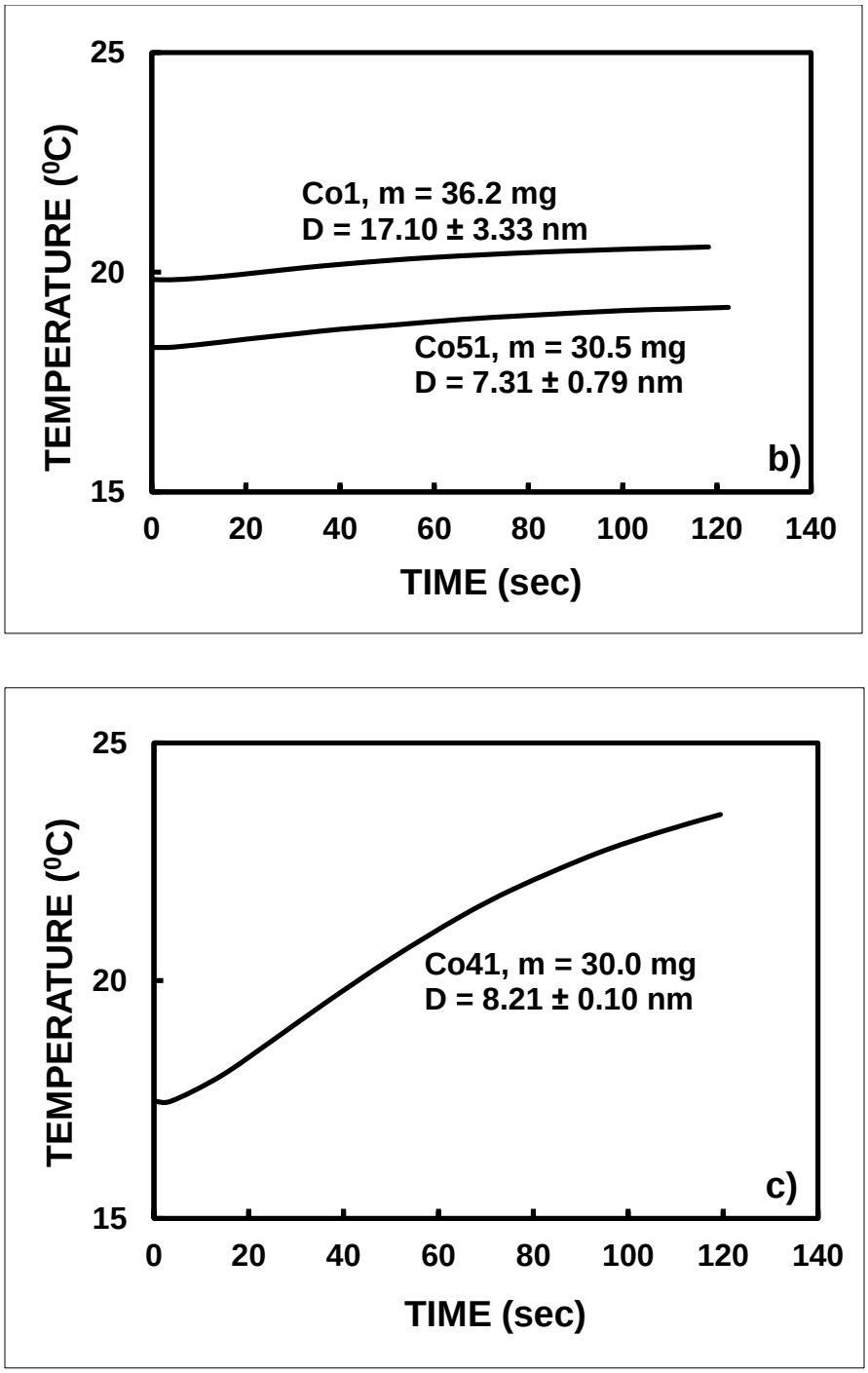

Figure 10. Heating curves for Co magnetic nanoparticles with different diameters (BKCo –).

nanoparticles about *18 nm* resulting in the highest temperature increase (ΔT) during heating process.

About *70%* of the human body is water. Therefore, its heat capacity can be approximated with the water's heat capacity to draw some conclusions with respect to magnetic hyperthermia treatment. Water has roughly four times higher heat capacity than air, see Table XI. Therefore, the changes in temperature during *100* seconds would be *4* times smaller if particles would be placed in water. For BKFe25, this would approximately mean that only a *3°C* change would occur in water. Assuming that the nanoparticles properties would not change in the environment of body temperature, which is *37°C* this would be too little a temperature change to achieve the therapeutically favored temperature of about *45°C* for the hyperthermia treatment. Of course, one could extend the time of the treatment, but the temperature gradient decreases with time and eventually saturate due to losses of heat to the environment. In our system, samples were vacuum isolated from all the sides, except of the top of the glass tube in which the sample was placed.

Sample name	Size [nm]	ΔT [°C]	Mass [mg]
BKFe25	18.6	~ 12.5	22.2
BKFe20	18.3	~ 11.5	23.6
BKFe10	8.0	~ 6	19.8
BKFe7	5.6	~ 2.5	26.3
BKFe6	11.3	~ 2.5	26.4
BKFe15	10.3	< 0.5	23.6

Table X. Fe magnetic nanoparticles with the highest increase in temperature (ΔT) during *100 s* heating process in ac magnetic field of $f = 174$ *kHz* and $B = 20.6\ \mu T$.

Substance	Heat capacity at 25 °C [J/gK]
Water	4.181
Air	1.012

Table XI. Comparison of heat capacity for water and air.

For cobalt nanoparticles the highest increase in temperature was about *5.5°C* for the sample BKCo41 with diameter of *8.21 nm*. This is important to stress that it is less than half of the increase achieved with BKFe25 which was also almost *7.8 mg* lighter. The curves for the cobalt nanoparticles in Fig. 10 are summarized in Table XII.

Sample name	Size [nm]	ΔT [°C]	Mass [mg]
BKCo41	8.2	~ 5.5	30.0
BKCo31	6.5	~ 1	14.8
BKCo51	7.3	~ 1	30.5
BKCo1	8.7	< 1	36.2
BKCo21	19.4	< 1	15.7

Table XII. Co magnetic nanoparticles with the highest increase in temperature (ΔT) during *100 s* heating process in ac magnetic field of $f = 174$ *kHz* and $B = 20.6\ \mu T$.

The heat rates using the Matlab code (Section 2.3) and the heating curves (see Appendix 1 and 2) for all the samples were found. Fig. 11 shows the typical dependence of the heat rate on the mass of the sample. This dependence is linear for BKCo41 and BKFe7 and nearly linear for BKCo31 and BKCo51.

Having calculated the heat rates, SLP and SLP' can be found using prescription given in Section 2.3. The highest values were found for exactly the same samples that had the highest increase in temperature and heat rate. All the values calculated are given in Appendix 1 and 2.

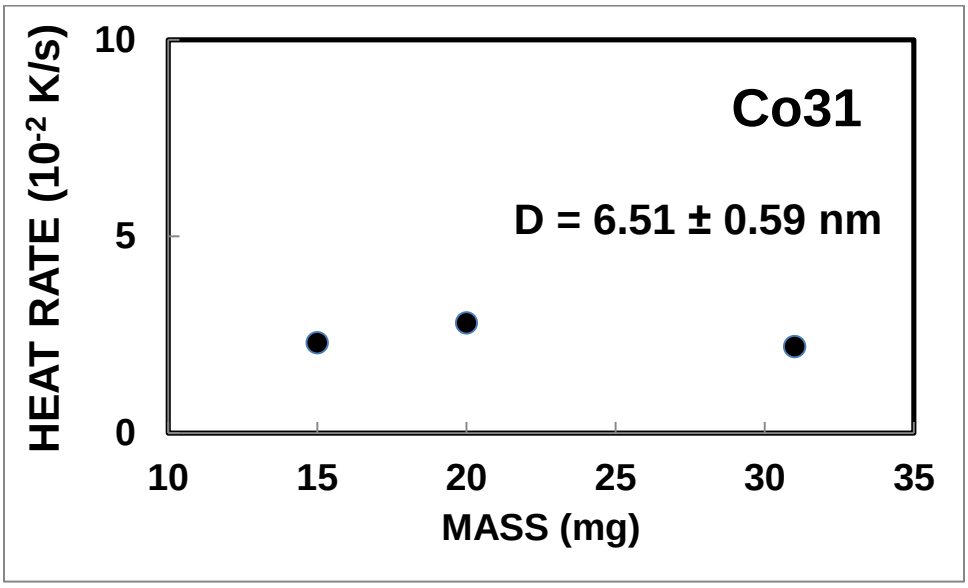
HEAT RATE (10-2 K/s)
10
5
0
Co31
D = 6.51 ± 0.59 nm
10
15
20
25
30
35
MASS (mg)

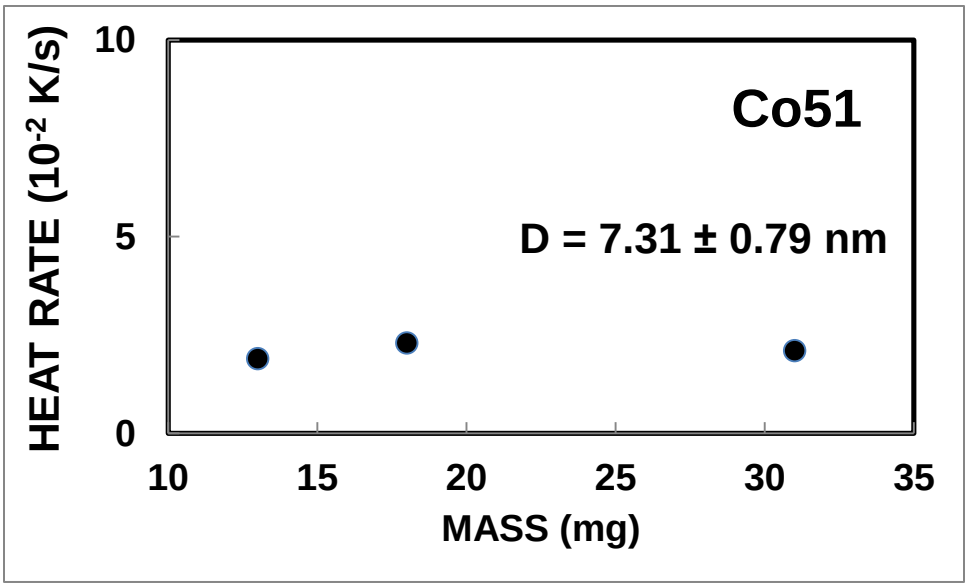
HEAT RATE (10-2 K/s)
10
5
0
Co51
D = 7.31 ± 0.79 nm
10
15
20
25
30
35
MASS (mg)

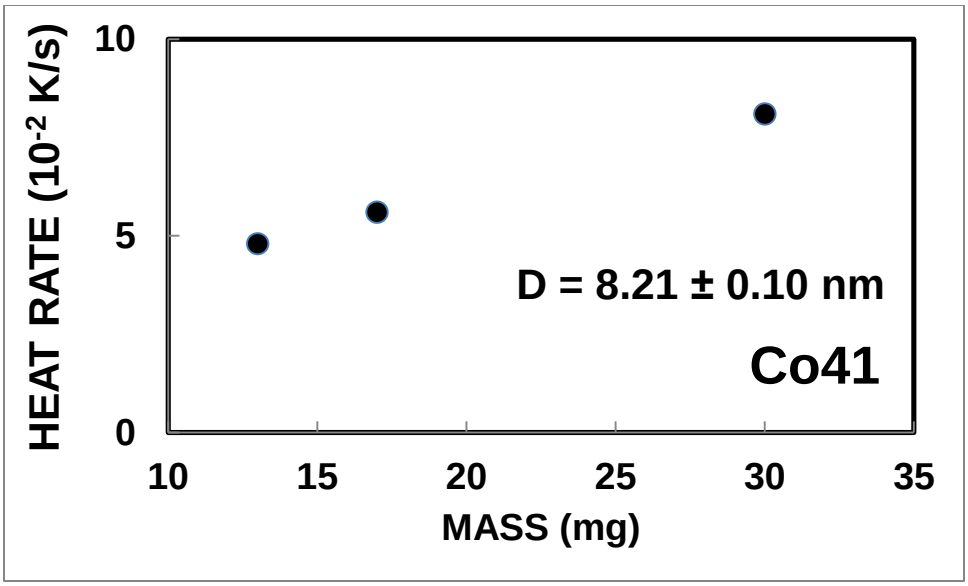

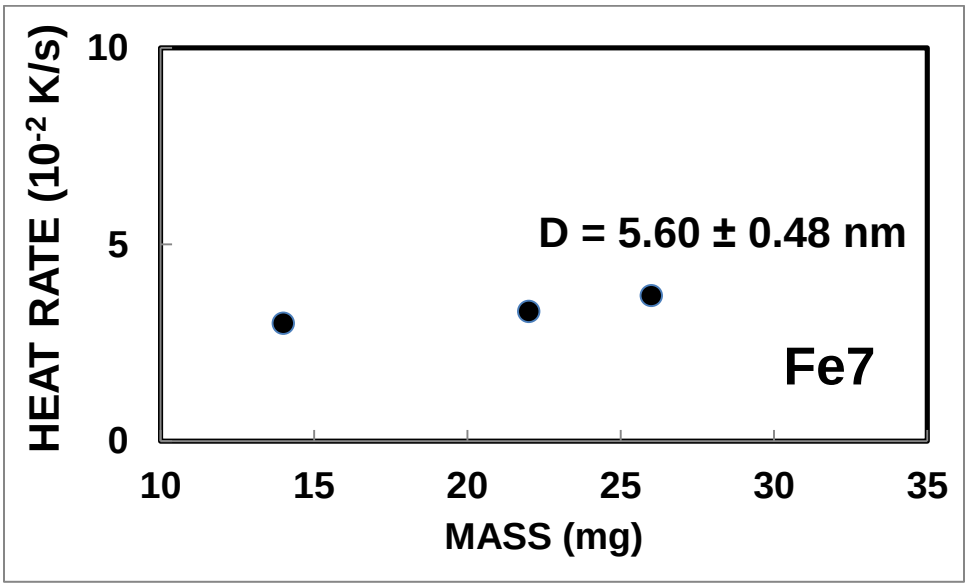

Figure 11. Heat rate versus mass for Co31, Co51, Co41, and Fe7 nanoparticles.

3.1.2 SLP' VERSUS DIAMETER

The coercivity H_c is a maximum at the critical diameter of the magnetic nanoparticles (Fig. 2) which is located at the transition from their multi- to single-domain

structure. A higher coercivity corresponds to a higher SLP values. Therefore, the mean particle diameter is a crucial parameter to maximize SLP. Since the mass of some of the samples was varied, SLP' = SLP/m_s was calculated for each measurement and this quantity was used to compare the samples to each other (see, Figs. 12 and 13). Approximated values of the critical diameters of iron and cobalt magnetic nanoparticles were determined using graphs in Figs. 12 and 13 since they have well defined maxima. The maximum specific loss power, SLP' = *1.557 W/g*^{2} was achieved for Co nanoparticle with *17.1 nm* in diameter (PACo1). The highest value of the specific loss power SLP'= *3.31 W/g*^{2} for Fe nanoparticles was achieved for the sample with a diameter of *18.61 nm* (BKFe25) (see, Fig. 13). The other local maximum in SLP' is observed in the range of nanoparticle diameter lying clearly in superparamagnetic regime (*D < 10 nm*, see Figs. 12-13).

The sample transition from multi-domain to single-domain and from single-domain to superparamagnetic regime (Table I) occur at critical diameters D_C and D_{SPM} (see Fig. 2). The superparamagnetic critical diameter D_{SPM} is expected to be between *8.21 nm* and *8.66 nm*, and a critical diameter for the transition from single to multi-domain regime D_c between *8.66 nm* and *19.42 nm* for the Co nanoparticle samples (Fig. 12). The D_{SPM} between *7.97 nm* and *10.31 nm* and a D_c between *18.61 nm* and *20 nm* are expected for the Fe nanoparticle samples (Fig. 13). The higher the SLP value is better for the hyperthermia application. The highest SLP' value was measured for BKFe25 with the *18.61 nm* diameter. The SLP'(BKFe25) = *3.3118 W/g*^{2} for a sample of mass of *22.0 mg* gives SLP(BKFe25) = *0.073 W/g*. The value of the SLP for a sample of iron oxide nanoparticles of approximately *18 nm* is taken from Fig. 5. It was measured in field with

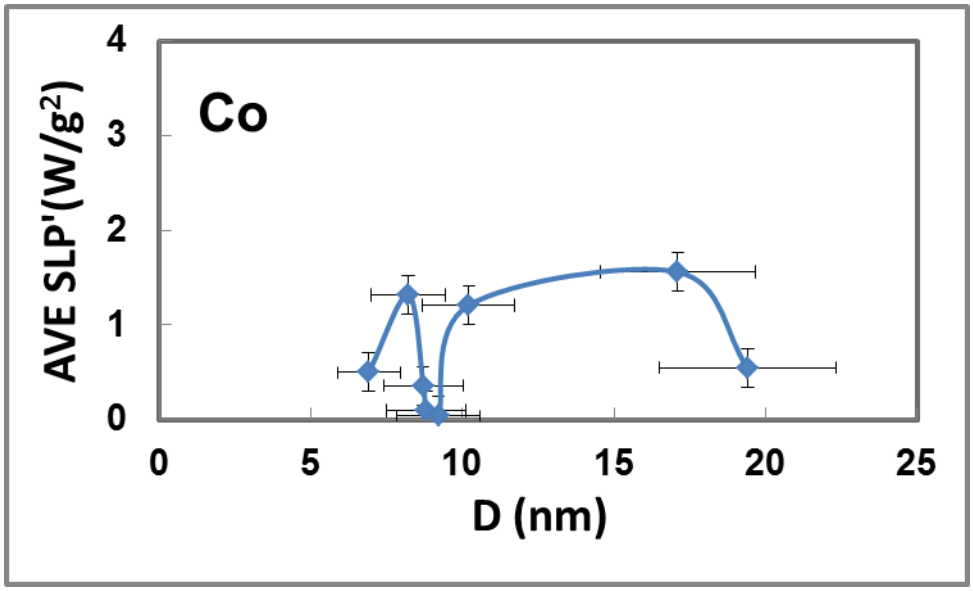

Figure 12. Average SLP' as a function of diameter for Co nanoparticles.

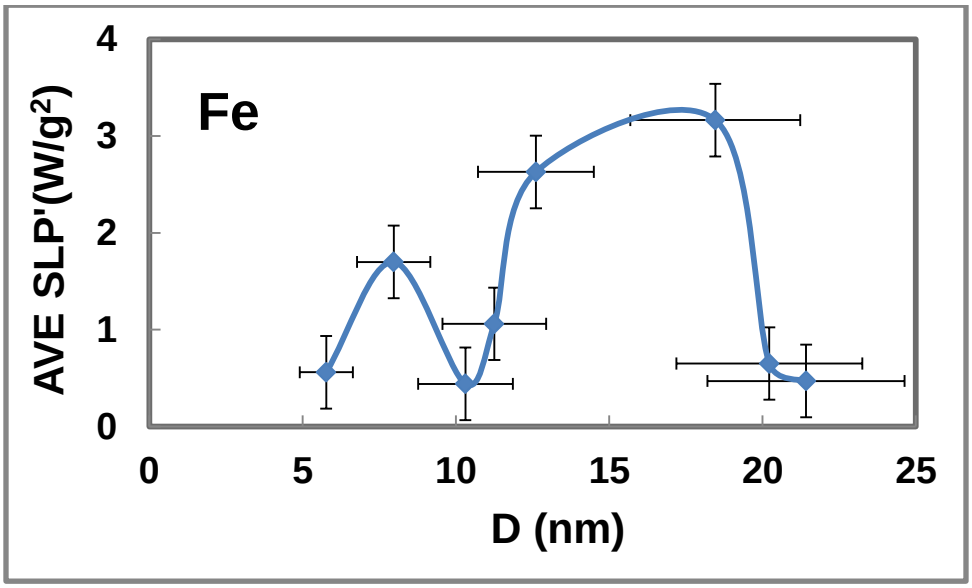

Figure 13. Average SLP' as a function of diameter for Fe nanoparticles.

frequency of *400 kHz* and amplitude *10 kA/m*. The SLP dependence on frequency in the regime from *100 kHz* to *400 kHz* is linear, and the dependence on field amplitude is

parabolic (goes as H^2) [38]. Therefore, the SLP value at frequency *174 kHz* and field amplitude *16.4 kA/m* can be calculated first by using linear law and then square law as follows: SLP (*174 kHz*) = *(174 kHz·180 W/g)/400 kHz = 78 W/g*, and SLP(*16.4 kA/m) = (78 W/g)/(10 kA/m)*^{2}*·(16.4 kA/m)*^{2} *= 207 W/g*. These results and data for BKFe25 are comparing a value of SLP for iron oxide in superparamagnetic regime [29] with our experimental result for pure iron taken clearly in the range of a second SLP peak's location related to the critical diameter D_C (transition from multi- to single-domain structure). This calculation and comparison result in a substantial discrepancy. By repeating the calculation for *D = 8 nm* (see, Fig. 5, [29]) with a value of SLP = *0.1 W/g* for superparamagnetic iron oxide and comparing our experimental result of SPL taken at the location of the first peak (Figs. 12-13) which happens to be SLP(BKFe10) = *0.03 W/g* for iron. This time, we can see from Table XIII that the SLP value for iron oxide is only slightly higher than our sample made of iron nanoparticles. This could be because of the fact that the iron nanoparticles were free to rotate and produce additional heat via Brown and Neel relaxations (Section 1.3.3). As a result, both mechanisms, which are important in superparamagnetic regime, contribute to heating with a maximum value of SPL at the crossover between Neelian and Brownian regimes. It is observed below critical diameter D_{SPM} (Figs. 12-13). The local minimum in Figs. 12-13 is an approximated value of D_{SPM} for Co and Fe magnetic nanoparticles.

3.2 HEAT MODEL

The heat model, based on Eq. 42 and 43, was successfully implemented for iron oxide in Matlab with values specified in Section 2.4. Fig. 14 is a 3D version of results

Name	D [nm]	f [kHz]	Field amplitude [kA/m]	SLP [W/g]
Magnetite [42]	8	150	5	0.11
Maghemite [42]	11	150	5	0.22
Iron [42]	6	150	5	0.70
Iron oxide [29]	8	174	16.4	0.12
BKFe10	8	174	16.4	0.03

Table XIII. SLP values for iron and iron oxide magnetic nanoparticles in superparamagnetic regime including BKFe10.

published by Chin-Tse Lin and Kuo-Chi Liu [35]. From Fig. 14, we can see that the highest increase of the temperature (the highest temperature is denoted by red color) is in the center of the tumor (where the radius is equal to zero). At the edge of the tumor, at radius of *0.005 m*, there is a drop in a temperature due to conduction of heat to healthy tissue that has originally temperature of *37°C* (denoted by blue color). Even though the whole volume of the tumor is uniformly filled with heat generating nanoparticles, the edges of the tumor will not be equally heated as the center of it. Also, we can see that healthy tissue from radius of *0.005* to *0.01 m* might be influenced by the temperature change generated in tumor if the experiment takes more than *1000* seconds. In this example, the increase in temperature caused by iron oxide nanoparticles with *19 nm* diameter was *2.4°C*. However, other doses of magnetic nanoparticles with the predetermined heating effect can be easily implemented. It could be a very useful tool for evaluating materials for hyperthermia treatment.

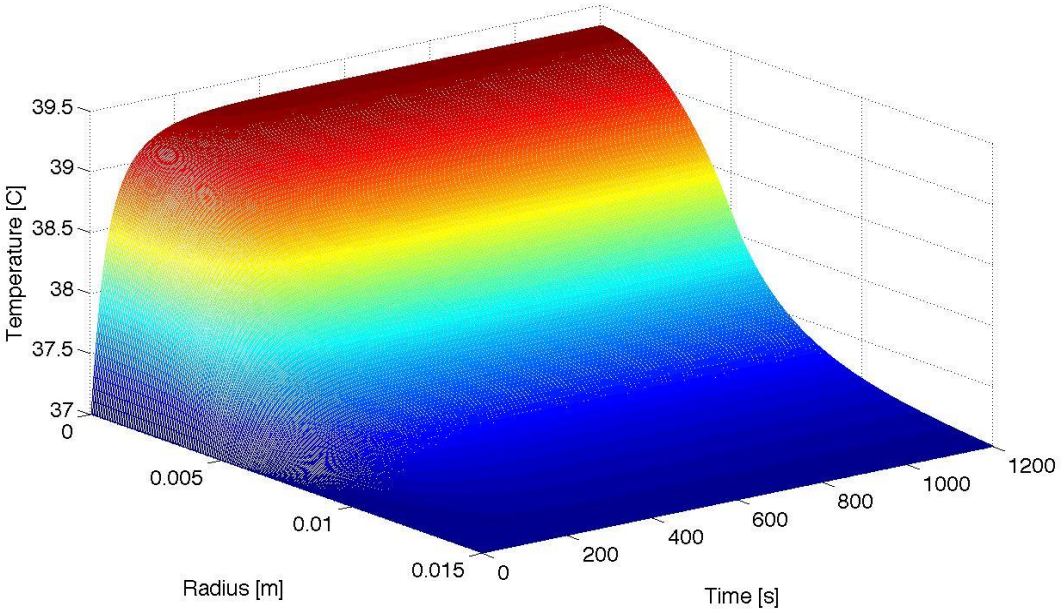

Figure 14. 3D plot of solution to heat equations for iron oxide of 19 nm in cancerous Eq. (42) and healthy Eq. (43) tissue [35], respectively.

4. CONCLUSIONS

During this project a better theoretical and experimental understanding of magnetic nanomaterials was acquired. Especially, nanomaterial's critical size behaviors when placed in an external ac magnetic field, and what requirements they have to fulfill to be a promising candidate for application in magnetic nanoparticle based hyperthermia treatment. The change in temperature for samples of iron and cobalt nanoparticles with different mean diameters *5.6 – 21.4 nm* for iron and *6.5 – 19.4 nm* were measured in an ac magnetic field. Heat curves and SLP' dependence on mean diameter were acquired. Measured nanoparticles were compared with the widely used iron oxide. A mathematical model for heat conduction from a tumor, filled with heat generating magnetic iron oxide nanoparticles, to healthy tissue was created and tested.

Main aim of thesis was to find an iron nanoparticle sample with a high enough SLP' value that could compete with the value achieved for iron oxide. The best sample found was BKFe25 with an approximately *18 nm* in diameter and SLP = *0.073 W/g*. When placed in air it gave an increase in temperature of approximately $12.5^{o}C$ during a *100 s* experiment. However, the heat power generated by this sample would not be satisfactory for a given amount to raise a human body temperature by $5\text{-}6^{o}C$, which is necessary to destroy cancer cells.

This project did find the critical diameters values for transitions from multi-domain to single-domain and from single-domain to superparamagnetic regime for iron and cobalt (see, Figs.12-13). It appears that SLP' versus diameter shows two local maxima and one minimum. First maximum at $D = 8.2\ nm$ for Co nanoparticles and $D = 8.0\ nm$ for Fe

nanoparticles is located in superparamagnetic regime where two mechanisms responsible for heating, namely Neelian and Brownian are contributing the most due to crossover between these two mechanisms. A minimum which appears roughly at *9 nm* for Co nanoparticles and *10 nm* for Fe nanoparticles is likely a first critical diameter D_{SPM} established at such dimensions of nanoparticles where coercivity in the sample starts to appear. This leads to a broad second maximum with a value of $D_c = 17.1\ nm$ for Co nanoparticles and $D_c = 18.3\ nm$ for Fe nanoparticles as a critical diameter values for transitions from single-domain to multi-domain which takes place at the maximum value of coercivity.

Our iron and cobalt nanoparticles were partially aggregated in clusters, which had substantial influence on heating curves. After all the data for this project have been acquired, we have discovered a method for size reduction of aggregated nanoparticles and we recommend it in future experiments. The method is to simply use a mortar and pestle to grind them thoroughly. However, particles meant for hyperthermia application should be analyzed if possible as a ferrofluid to achieve a better understanding of what heat they would produce in human tissue environment.

The Matlab constructed mathematical model did successfully solve the bio-heat equations for cancerous and healthy tissue, and gave a temperature profile for spherical tumor surrounded by healthy tissue as a function of radius and time. The model also can be utilized to estimate the minimum amount of material that is to be injected to tumor to achieve desired increase of temperature without overheating the neighboring healthy tissue.

5. REFERENCES

[1] P. Abdulkin, T. Houlding, B.R. Knappett, A.B. Lukawska, V. Degirmenci, D.A. Jefferson, G. Kozlowski, E.V. Rebrov, and A.E.H. Wheatley, "Synthesis and Size Control in Magnetically Active Fe and Co Nanoparticle Systems", in preparation.

[2] P. Milde, D. Kohler, J. Seidel, L.M. Eng, A. Bauer, A, Chason, J. Kindervater, S. Muhlbauer, C. Pfleiderer, S. Buhrandt, C. Schutte, and A. Rosch, "Unwinding of a Skyrmion Lattice by Magnetic Monopoles", Science, 340 (2013) 6136.

[3] http://en.wikipedia.org/wiki/Permeability (Electromagnetism).

[4] http://en.wikipedia.org/wiki/Magnetization.

[5] M. Getzlaff, Fundamentals of Magnetism, Springer-Verlag, Berlin-Heidelberg, 2008.

[6] R.F. Butler, Paleomagnetism: Magnetic Domains to Geologic Terranes, Blackwell Scientific Publications, Boston, MA, 1992.

[7] O. P. Pahuja, Solid State Physics, Laxmi Publications LTD, New Delhi, 2005.

[8] E.Y. Tsymbal, "Magnetic Properties of Materials", (http://physics.unl.edu /tsymbal/teaching/SSP-927/Section_2015_Magnetic_Properties_1.pdf).

[9] M.Z. Jagoo, Radio-frequency Heating of Magnetic Nanoparticles, Master Thesis, OhioLink, WSU, 2012.

[10] E.Y. Tsymbal, “Magnetic Properties of Materials”, (http://physics.unl.edu /tsymbal/teaching/SSP927/Section_2015_Magnetic_Properties_2.pdf).

[11] A.H. Lu, E.L. Salabas, and F. Schuth, “Magnetic Nanoparticles: Synthesis, Protection, Functionalization, and Application”, Angewandte Chemie International Edition, 46 (2007) 1222.

[12] C.G. Stefanita, Magnetism, Springer-Verlag, Berlin-Heidelberg, 2012.

[13] J. Sólyom, Fundamentals of the Physics of Solids, “Magnetically Ordered Systems”, 1 (2007) 449.

[14] http://en.wikipedia.org/wiki/Antiferromagnetism.

[15] A.P. Guimaraes, Principles of Nanomagnetism, Springer-Verlag, Berlin-Heidelberg, 2009.

[16] J. Neamtu and N. Verga, “Magnetic Nanoparticles for Magneto-resonance Imaging and Targeted Drug Delivery”, Digest Journal of Nanomaterials and Biostructures, 6 (2011) 969.

[17] J.M.D. Coey, “Magnetism in Future”, Journal of Magnetism and Magnetic Materials, 226-230 (2001) 2107.

[18] N.T.K. Thanh, Magnetic Nanoparticles: From Fabrication to Clinical Application, CRC Press, Boca Raton, FL, USA, 2012.

[19] L. Tauxe, Essentials of Paleomagnetism, University of California Press, 2010.

[20] J. Carvell, E. Ayieta, A. Gavrin, R.H. Cheng, V.R. Shah, and P. Sokol, Magnetic Properties of Iron Nanoparticles, Journal of Applied Physics 107 (2010) 103919.

[21] B. M. Moskowitz, Hitchhiker’s Guide to Magnetism, Environmental Magnetism Workshop, Minneapolis, 1991.

[22] R. Hergt, S. Dutz, R. Müller, and M. Zeisberger, "Magnetic Particle Hyperthermia: Nanoparticle Magnetism and Materials Development for Cancer Therapy", J. Phys.: Condens. Matter, 18 (2006) S2919.

[23] R. Hergt, S. Dutz, and M. Roder, "Effects of Size Distribution on Hysteresis Losses of Magnetic Nanoparticles for Hyperthermia," J. Phys.: Condens. Matter, 20 (2008) 385214.

[24] http://en.wikipedia.org/wiki/Magnetic_Domain.

[25] S. Kasap, Principles of Electronic Materials and Devices, Third Edition, McGraw-Hill, 2006.

[26] W.D. Callister, Jr., Materials Science and Engineering: Introduction, John Wiley & Sons, Chapter 20, 2007.

[27] W.D. Callister, Jr, "Materials Science and Engineering: Introduction", John Wiley & Sons, Chapter 20, Fig 20.13, 2007.

[28] R. Hergt, S. Dutz, R. Muller, and M. Zeisberger, "Magnetic Particle Hyperthermia: Nanoparticle Magnetism and Materials Development for Cancer Therapy", J. Phys.: Condens. Matter, 18 (2006) S2919, 21 (2005) 637.

[29] W. Andra and H. Nowak, Magnetism in Medicine. A Handbook, Chapter 4.6: "Magnetic Hyperthermia and Thermoablation" by R. Hergt and W. Andra, Second Edition, WILEY-VCH, 2007.

[30] http://en.wikipedia.org/wiki/William_Coley.

[31] A. Jordan, R. Scholz, K. Maier-Hauff, M. Johannsen, P. Wust, J. Nadobny, H. Schirra, H. Schmidt, S. Deger, S. Loening, W. Lanksch, and R. Felix, "Presentation of a New Magnetic Field Therapy System for the Treatment of

Human Solid Tumors with Magnetic Fluid Hyperthermia", Journal of Magnetism and Magnetic Materials, 225 (2001) 118.

[32] M. Johannsen, B. Thiesen, P. Wurst, and A. Jordan, "Clinical Hyperthermia of Prostate Cancer Using Magnetic Nanoparticles: Presentation of a New Interstitial Technique", Int. J. Hyperthermia, 21(2005) 637.

[33] http://www.magforce.de/(from 14th March 2014).

[34] K. Maier-Hauff, F. Ulrich, D. Nestler, H. Niehoff, P. Wust, B. Thiesen, H. Orawa, V. Budach, and A. Jordan, "Efficacy and Safety of Intratumoral Thermotherapy Using Magnetic Iron-oxide Nanoparticles Combined with External Beam Radiotherapy on Patients with Recurrent Glioblastoma Multiforme", J. Neurooncol., 103 (2011) 317.

[35] C.T. Lin and K.C. Liu, "Estimation for the Heating Effect of Magnetic Nanoparticles in Perfused Tissues," International Communications in Heat and Mass Transfer, 36 (2009) 241.

[36] A.B. Lukawska, Z. Jagoo, G. Kozlowski, Z. Turgut, H. Kosai, A. Sheets, T. Bixel, A. Wheatley, P. Abdulkin, B. Knappett, T. Houlding, and V. Degirmenci, "Ac Magnetic Heating of Superparamagnetic Fe and Co Nanoparticles", Defect and Diffusion Forum, 336 (2013) 159.

[37] http://www.fiso.com/admin/useruploads/files/fot-l.pdf.

[38] R. Hergt, R. Hiergeist, I. Hilger, W.A. Kaiser, Y. Lapatnikov, S. Margel, and U. Richter, "Maghemite Nanoparticles with Very High AC-losses for Application in RF-magnetic Hyperthermia", Journal of Magnetism and Magnetic Materials, 270

(2004) 345.

[39] http://www.irm.umn.edu/hg2m/hg2m_b/hg2m_b.html.

[40] http://en.wikipedia.org/wiki/Reflux.

[41] H.M. Lu, W.T. Zheng, and Q. Jiang, "Saturation Magnetization of Ferromagnetic and Ferromagnetic Nanocrystals at Room Temperature", J. Phys. D: Appl. Phys., 40 (2007) 320.

[42] W.J. Winkowycz, E.M. Sparrow, and J.P. Abraham, "Nanoparticle Heat Transfer and Fluid Flow", CRC Press, Taylor&Francis Group, Boca Raton, London, New York, 2013.

APPENDIX 1

Sample Name	Size [nm]	± SizeError [nm]	Weight [g]	Heat rate [K/s]	SLP [W/g]	SLP' [W/g^2]	Ave_SLP' [W/g^2]	sd(SLP') [W/g^2]	Ave_SLP [W/g]	sd(SLP) [W/g]
BKFe10	7.97	1.52	0.0198	0.0764	0.0344	1.7379	1.6992	0.0631	0.0336	0.0009
			0.0198	0.0715	0.0322	1.6264				
			0.0198	0.0762	0.0343	1.7334				
BKFe15	10.31	1.83	0.0236	0.0213	0.0096	0.4065	0.4383	0.0358	0.0103	0.0006
			0.0236	0.025	0.0113	0.4771				
			0.0236	0.0226	0.0102	0.4313				
BKFe20	18.31	1.95	0.0236	0.1548	0.0697	2.9543	3.0186	0.0937	0.0712	0.0016
			0.0236	0.1559	0.0702	2.9753				
			0.0236	0.1638	0.0738	3.1261				
BKFe25	18.61	1.97	0.022	0.1604	0.0722	3.2838	3.3118	0.0689	0.0729	0.0011
			0.022	0.1656	0.0746	3.3903				
			0.022	0.1593	0.0717	3.2613				
BKFe5	20	1.27	0.0236	0.0186	0.0084	0.3550	0.7391	-	-	-
			0.0162	0.0404	0.0182	1.1232				
BKFe6	11.25	1.4	0.0265	0.0628	0.0283	1.0674	1.0576	0.2708	-	-
			0.0265	0.0605	0.0272	1.0283				
			0.0129	0.0371	0.0167	1.2953				
			0.0264	0.0492	0.0222	0.8394				
BKFe7	5.6	0.48	0.0219	0.0332	0.0150	0.6828	0.7719	0.1969	-	-
			0.0135	0.0299	0.0135	0.9976				
			0.0263	0.0371	0.0167	0.6354				
PTFe2	21.44	1.73	0.0309	0.045	0.0203	0.6559	0.6194	0.0479	-	-
			0.0309	0.0422	0.0190	0.6151				
			0.0309	0.0435	0.0196	0.6341				
			0.0387	0.0492	0.0222	0.5726				
PTFe03	12.61	1.62	0.1099	1.1136	0.5016	4.5638	2.6287	2.8182	-	-
			0.1099	0.9066	0.4083	3.7155				
			0.1099	0.3466	0.1561	1.4205				
			0.1099	0.346	0.1558	1.4180				
			0.0392	0.1763	0.0794	2.0257				

APPENDIX 2

Sample Name	Size [nm]	± Size Error	Weight [g]	Heat rate [K/s]	SLP [W/g]	SLP' [W/g^2]	Ave_SLP' [W/g^2]	sd(SLP') [W/g^2]	Ave_SLP [W/g]	sd(SLP) [W/g]
BKCo1	8.66	1.22	0.0159	0.0187	0.0079	0.4937	0.3582	-	-	-
			0.0362	0.0192	0.0081	0.2227				
BKCo21	19.42	4.45	0.0157	0.0206	0.0086	0.5508	0.5508	-	0.0086	-
BKCo31	6.51	0.59	0.0204	0.0282	0.0118	0.5803	0.5139	0.1891	-	-
			0.031	0.0222	0.0093	0.3006				
			0.0148	0.0233	0.0098	0.6609				
BKCo41	8.21	0.104	0.0125	0.0484	0.0203	1.6255	1.3231	0.4171	-	-
			0.0172	0.0507	0.0213	1.2374				
			0.0172	0.0615	0.0258	1.5010				
			0.03	0.0818	0.0343	1.1447				
			0.03	0.0791	0.0332	1.1069				
BKCo51	7.31	0.78	0.018	0.0233	0.0098	0.5434	0.4813	0.1661	-	-
			0.0132	0.0191	0.0080	0.6074				
			0.0305	0.0213	0.0089	0.2932				
PACo9	9.23	1.26	0.1716	0.0191	0.0080	0.0467	0.0357	0.0263	-	-
			0.1716	0.0156	0.0065	0.0382				
			0.1716	0.0195	0.0082	0.0477				
			0.1716	0.0187	0.0079	0.0457				
			0.0387	0	0.0000	0.0000				
PACo8	8.84	0.65	0.1279	0.0284	0.0119	0.0932	0.1037	0.0866	-	-
			0.1279	0.0223	0.0094	0.0732				
			0.1279	0.0214	0.0090	0.0702				
			0.1279	0.0235	0.0099	0.0771				
			0.1279	0.0217	0.0091	0.0712				
			0.0391	0.0221	0.0093	0.2373				
PACo2	10.19	1.08	0.0899	0.2302	0.0966	1.0749	1.2092	0.3006	-	-
			0.0899	0.2398	0.1007	1.1198				
			0.0899	0.2729	0.1146	1.2743				
			0.0899	0.2787	0.1170	1.3014				
			0.0899	0.3054	0.1282	1.4261				
			0.0389	0.0981	0.0412	1.0587				
PACo1	17.1	3.33	0.1326	0.6184	0.2596	1.9578	1.5557	0.4322	-	-
			0.1326	0.4674	0.1962	1.4797				
			0.1326	0.466	0.1956	1.4753				
			0.1326	0.4842	0.2033	1.5329				
			0.0394	0.1251	0.0525	1.3329				

LIST OF SYMBOLS, ABBREVIATIONS, AND ACRONYMS

Acronym	**Description**
NPs	Nanoparticles
NP	Nanoparticle
MNPs	Magnetic Nanoparticles
SLP	Specific Loss Power
WSU	Wright State University
WPAFB	Wright-Patterson Air Force Base
AFRL	Air Force Research Laboratory

LIST OF CONFERENCE PRESENTATIONS AND ATTENDANCE DURING MASTER STUDY AT WSU

May 9-11, 2012	International Conference on Materials, Energy and Environment (ICMEE)	Toledo, OH	Attendance
April 13-14, 2012	Spring Meeting - Biophysics, (OSAPS)	The Ohio State University, Columbus, OH	Poster presentation: Interrogation of $Co_xZn_yNi_{1-x-y}Fe_2O_4$ ferrite nanoparticles for insight into specific power loss for medical hyperthermia, Zafrullah Jagoo, Anna Lukawska and Gregory Kozlowski
June 25-29, 2012	8th International Conference on Diffusion in Solids and Liquids (DSL2012)	Istanbul, Turkey	Invited talk:Ac magnetic heating of superparamagnetic Fe and Co nanoparticles, Zafrullah Jagoo, Anna Lukawska, Gregory Kozlowski, Zafer Turgut, Hiroyuki Kosai, Alexander Sheets, Tyler Bixel, Andrew Wheatley, Pavel Abdulkin and Thomas Houlding
July 23, 2012	Leibniz Institute for Solid State and Research	Dresden, Germany	Invited talk: Ac Magnetic Heating of Superparamagnetic Fe and Co Nanoparticles for Application in Hyperthermia, Anna Lukawska, Zafrullah Jagoo, Gregory Kozlowski, Zafer Turgut, Hiroyuki Kosai, Alexander Sheets, Tyler Bixel, Andrew Wheatley, Pavel Abdulkin, Benjamin Knappett,Thomas Houlding and Volkan Degirmenci
August 7-9, 2012	3rd International Conference on Nanotechnology: Fundamentals and Applications, ASET	Montreal, Canada	Oral presentation:RF Heating Characteristics and Magnetic Properties of Solid Colloidal FePt Nanoparticles, Anna Lukawska, Zafrullah Jagoo, Gregory Kozlowski, Zafer Turgut, Hiroyuki Kosai, Alexander Sheets, Tyler Bixel and Andrew Wheatley
November 5-6, 2012	The 2012 Nanotechnology Materials and Devices (NMD) Workshop	Dayton, OH	Attendance
November 16, 2012	AIHA November Meeting (Chuck Geraci, Ph.D.: An update from Helsinki: Nanomaterial Sampling Harmonization)	Cincinnati, OH	Attendance
November 28, 2012	Hazardous waste operations and emergency response (HAZWOPER) training	Wright State University, Dayton, OH	Attendance
January 14-18, 2013	12th Joint MMM-Intermag Conference	Chicago, IL	Attendance
June 24-28, 2013	9th International Conference on Diffusion in Solids and Liquids (DSL2013)	Madrid, Spain	Invited talk: Heating mechanisms of magnetic nanoparticles in hyperthermia treatment, Anna Lukawska and Gregory Kozlowski